DETECTION AND ESTIMATION OF OBJECTS FROM NOISY PROJECTION MEASUREMENTS

by

Daniel Mark Spielman

SUBMITTED TO THE DEPARTMENT OF ELECTRICAL ENGINEERING IN PARTIAL FULFILLMENT OF THE REQUIREMENTS FOR THE DEGREE OF

BACHELOR OF SCIENCE

at the

MASSACHUSETTS INSTITUTE OF TECHNOLOGY

May 1983

Copyright © 1983 Massachusetts Institute of Technology

Signature of Author _____

Department of Electrical Engineering
May 20, 1983

Certified by _____

Alan S. Willsky
Thesis Supervisor

Accepted by _____

Chairman, Departmental Committee on Theses

Detection and Estimation of Objects from Noisy Projection Measurements

by

Daniel Mark Spielman

Submitted to the Department of Electrical Engineering on May 20, 1983 in partial fulfillment of the requirements for the degree of Bachelor of Science.

Abstract

The problem of reconstructing a cross-sectional density function using noisy projection measurements is considered. Using a stochastic formulation, an iterative procedure for detecting and estimating finitely paramaterized objects is described. Computer simulations are then used to analyze the performance of this algorithm for density fields consisting of single as well as multiple objects.

Thesis Supervisor: Alan S. Willsky
Title: Associate Professor of Electrical Engineering

Acknowledgments

I would first like to express my deepest appreciation to Professor Alan Willsky. His guidance, expertise, and enthusiasm made this work possible. Second, I would like to thank David Rossi whose doctoral work formed the foundation for this thesis.

In addition, I express gratitude to Stephen Cole for his support and encouragement. And finally, a special thank you to Frances Sun. Her many long distance phone calls kept my spirits up and pencil writing.

Table of Contents

List of Figures

List of Tables

Chapter 1
Introduction

The general problem of tomography, the reconstruction of multidimensional functions from measurements of line integrals of these functions, has been well-studied and has many applications. The problem can be stated mathematically as follows: let $f(\mathbf{x})$ be a function where $\mathbf{x}$ is an n-dimensional vector defined in some region of $\mathbf{R}^n$. From noisy measurements along a (possibly infinite) set of lines L_i,

$$g(L_i)=\int_{L_i} f(\mathbf{x})ds \tag{1.1}$$

the goal is to reconstruct the function $f(\mathbf{x})$. Thus, given the set of line integrals $g(L_i)$, known as projection measurements, the problem is to find the best estimate $\hat{f}(\mathbf{x})$ of the function $f(\mathbf{x})$.

Tomography is used in a wide variety of disciplines, medical applications being perhaps the best known. Both Computerized Axial Tomography (CAT) scanners and ultrasound devices are widely used medical diagnostic tools which produce 2-dimensional cross sectional images. CAT scanners employ reconstruction based on the fact that X-ray attenuation in biological tissue can be directly related to the line integral of the X-ray absorption density, while unltrasound devices use time-of-flight measurements to provide path integrals of the tissue refractive index. In addition, emissions from injections of radionuclides into the body form the basis of various passive reconstruction techniques.

There are also numerous non-medical applications. Reconstruction is used extensively for energy resource mapping in the geophysics industry. Oceanographers exploit the fact that the propagation velocity of sound in water is temperature dependent to reconstruct underwater temperature profiles. Other applications of tomography include problems in electron microscopy, radio astronomy, meteorology, target estimation, and non-destructive testing.

The ideal case reconstruction problem, in which a set of noise-free integrals are taken at all angles, was solved exactly by J. Radon (1917). However, real world applications never achieve this level of perfection or completeness. Measurements contain some noise and can only be taken from a finite number of orientations. For example, ultrasound images tend to be very noisy because the sound travels through the body in curved rather than straight paths.

Present techniques attempt to reconstruct the most complete representation of $f(\mathbf{x})$ possible. Using all of the available data, a high resolution image is formed. This type of reconstruction involves solving for a very large number of unknowns and requires taking many accurate measurements.

However, in many applications, the ultimate goal is not necessarily a high quality picture, but rather the extraction of some specific information, such as the presence of a tumor or the shape of a bone. Oil companies, for example, are not interested in an arbitrarily detailed description of some section of the ground, but only the existence of various distinguishable layers. Often, to enhance the important aspects of the picture, a significant amount of post-processing is performed. Medical CAT scan images are frequently processed to delineate the boundaries of bones, organs, tumors, or fluid regions.

The reconstruction methods currently being used are not tailored to applications where the true aim is not a high resolution, high quality picture, but rather the more modest goal of extracting specific details from the image. Post-processing is used to highlight the desired data. This additional processing can essentially be viewed as the incorporation of a priori information. Yet, this processing is performed only after the image has been reconstructed.

The incorporation of this a priori knowledge into the reconstruction process itself, in some sense, reduces the number of unknowns of the problem. With fewer degrees of freedom, equal or better performance should be obtainable with less or noiser data. An algorithm of this type has some significant advantages. The major limitation of current reconstruction techniques is the requirement of large amount of data taken with a very high signal-to-noise ratio (SNR). Taking this amount of relatively noise-free data is often difficult, expensive, and/or undesirable. The high X-ray dosages associated with CAT scans is an excellent example of an expensive, undesirable consequence of the substantial data requirements of convential methods. Oceanography and geophysics provide examples in which meeting such requirements are, for all practical purposes, impossible.

The problem of incoporating a priori information into the reconstruction problem using an object-based stochastic formulation was analyzed by David Rossi (1982). Objects were characterized by a finite number of parameters (location, size, eccentricity, and orientation), and these parameters were estimated from the original projection data using a maximum likelihood technique. Performance bounds were derived, and algorithms were suggested. The key aspect of Rossi's work was that, using a priori information, the

reconstruction process was optimized in terms of the accuracy and reliability of object detection and estimation, not image quality.

This thesis is an extension of the work done by Rossi. Chapter 2 is an introduction to the object-based reconstruction technique leading to an iterative algorithm for object detection and estimation (chapter 3). In chapters 4 and 5, computer simulations are used to analyze the performance of this algorithm for single and multiple object fields.

Chapter 2
Object Based Reconstruction

2.1 The Radon Transform

In order to discuss reconstruction, the geometry of the problem must be specified. Let $f(\mathbf{x})$, the function to be estimated, be defined in some region of $\mathbf{R}^2$. Projection lines through this region are parameterized by an angle θ and distance t from the origin (see figure 2.1). In terms of the Cartesian coordinates x_1, and x_2, the line $l(t,\theta)$ is expressed as

$$l(t,\theta) \equiv \left\{ \mathbf{x}=(x_1,x_2) | x_1\cos\theta + x_2\sin\theta = t \right\} \tag{2.1}$$

where

$$-\infty < t < \infty \text{ and } 0 < \theta < \pi.$$

In general, the extent of $f(\mathbf{x})$ in any application is bounded, and in the computer simulations presented later in this thesis we restrict the support region of $f(\mathbf{x})$ to be of radius T=50, i.e.

$$f(\mathbf{x}) = 0 \text{ if } \|\mathbf{x}\| > T = 50. \tag{2.2}$$

The integral of $f(\mathbf{x})$ along the projection $l(t,\theta)$ is denoted by $g(t,\theta)$ and is known as the *Radon transform* of $f(\mathbf{x})$. Thus for given values of t and θ:

$$g(t,\theta) = \int_{-\infty}^{\infty} \int_{-\infty}^{\infty} f(\mathbf{x}) \delta(t - x_1\cos\theta - x_2\sin\theta) dx_1 dx_2 \tag{2.3}$$

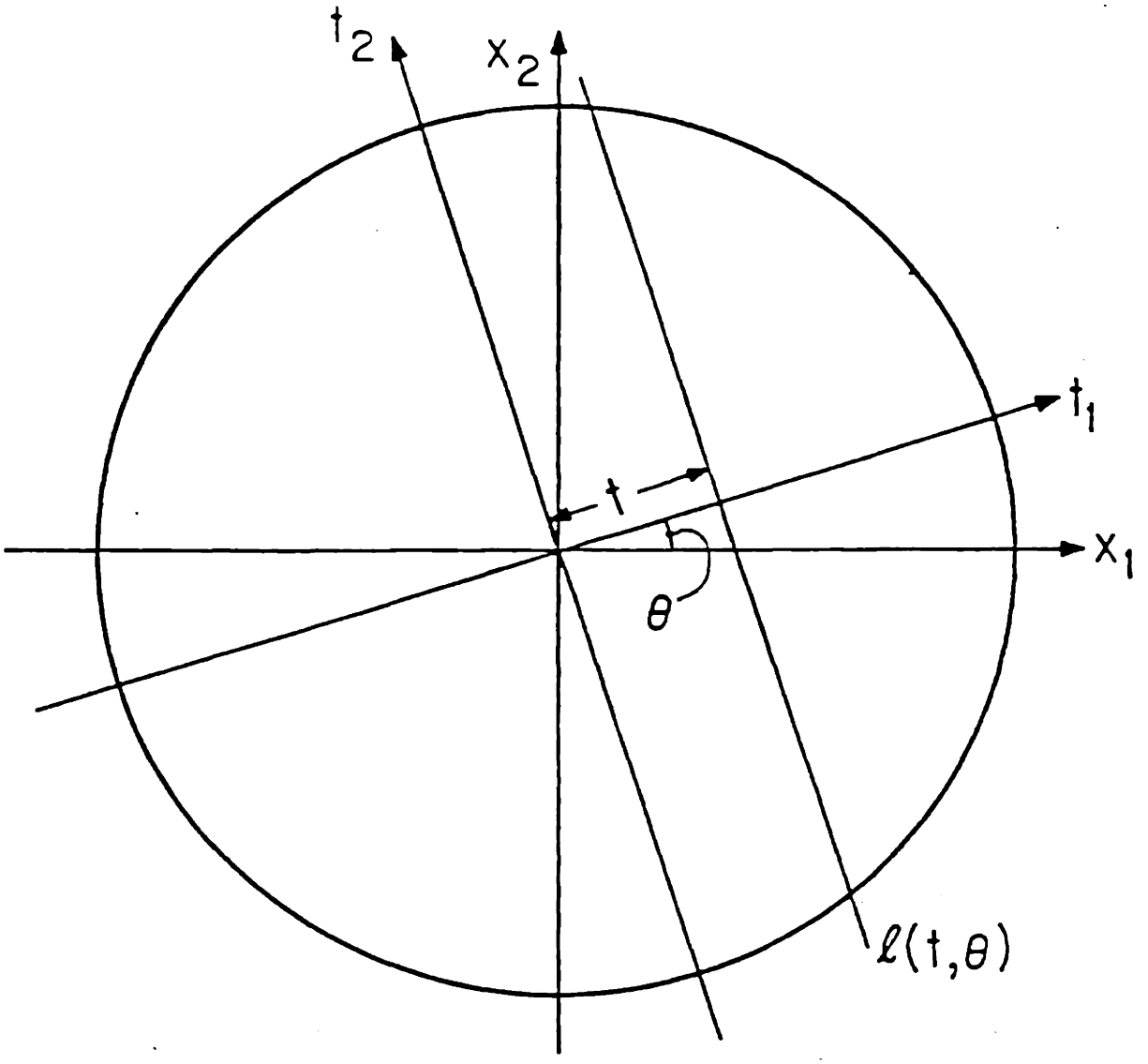

Figure 2-1: Measurement geometry.

$$= \int_{l(t,\theta)} f(\mathbf{x}) ds$$

where δ is the Dirac Delta function.

Some of the properties of the Radon transform are best illustrated with an example. Let $f(\mathbf{x})$ take some constant non-zero value on a square region centered at $\mathbf{c}$ and be zero everywhere else. Then, the Radon transform for a fixed θ is trapazoidal (see figure 2.2), and the shape of this trapazoid varies with different values of θ. Figure 2.3 shows that the centroid of the square traces a sinusoidal curve in Radon space. In general, the Radon transform of the centroid of any object forms a sinusoidal curve whose amplitude and phase are determined by the object's location. Thus, determining the object location involves estimating this sinusoidal shift.

2.2 Present Reconstruction Algorithms

Current reconstruction techniques essentially fall into two catagories: discrete approaches, and the *convolution back-projection* algorithms. A brief discussion of these two methods is given here in order to point out the differences and similarities between these reconstruction algorithms and the object-based one used in this thesis.

The discrete algorithm breaks the region $\|\mathbf{x}\|<T$ into small pixels over which $f(\mathbf{x})$ is assumed to be constant. Under this assumption, $g(t,\theta)$ is viewed as a sum of discrete contributions weighted by the chord length of intersection of the line $l(t,\theta)$ and a particular pixel. This results in a set of linear equations of the form

$$\mathbf{g}=\mathbf{H}\mathbf{f} \qquad (2.4)$$

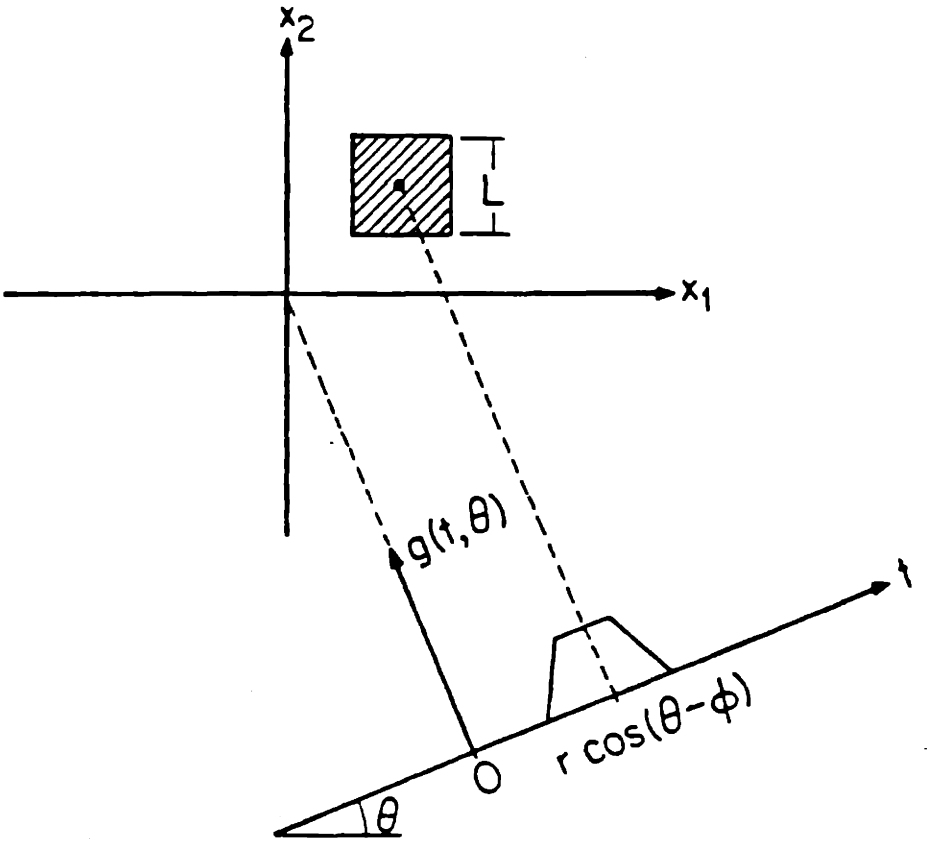

Figure 2-2: Projection at angle θ.

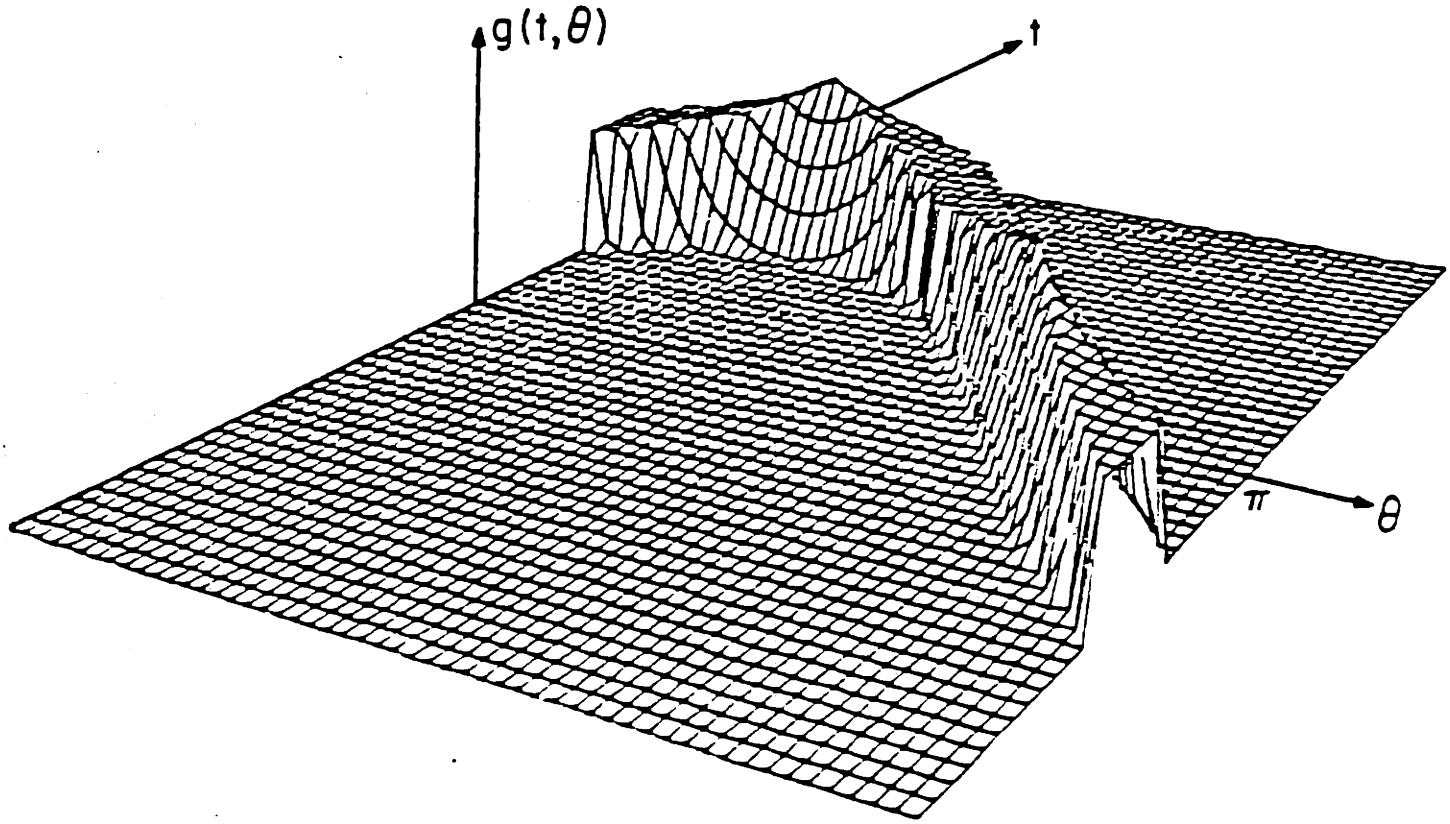

Figure 2-3: Radon transform of single box object.

where f is the vector of pixel values of $f(\mathbf{x})$. Reconstruction algorithms focus on inverting the matrix **H** in order to solve for f.

The convolution back-projection algorithm makes use of the Fourier transform of $g(t,\theta)$:

$$G(\omega,\theta)=\int_{-\infty}^{\infty} e^{-i\omega t} g(t,\theta)dt. \tag{2.5}$$

Noting that $G(\omega,\theta)$ is equal to the two-dimensional Fourier transform of f in polar coordinates:

$$G(\omega,\theta)=f(\omega,\theta)=\int_{-\infty}^{\infty}\int_{-\infty}^{\infty} f(\mathbf{x})e^{-i\omega(x_1\cos\theta+x_2\sin\theta)}dx_1dx_2 \tag{2.6}$$

the function $f(\mathbf{x})$ can be found using the Fourier inversion formula. Namely:

$$f(\mathbf{x})=\frac{1}{4\pi^2}\int_0^{\pi} d\theta \int_{-\infty}^{\infty} G(\omega,\theta)e^{i\omega(x_1\cos\theta+x_2\sin\theta)}|\omega|d\omega \tag{2.7}$$

where $|\omega|$ is the Jacobian resulting from the conversion to polar coordinates.

Equation 2.7 can be reduced to what is known as the convolution back-projection (CBP) inversion formula:

$$f(\mathbf{x})=\int_0^{\pi}\int_{-\infty}^{\infty} g(t,\theta)v(t-\tau(\mathbf{x},\theta))dtd\theta \tag{2.8}$$

where the Fourier transform of v(t) is $V(\omega)=|\omega|$ and $\tau=x_1\cos\theta+x_2\sin\theta$. In actual applications these integrals are replaced by finite sums and the function v(t), known as the kernel, is chosen on the basis of a noise-resolution tradeoff.

The CBP inversion formula has a relatively intuitive interpretation. The back projection operation invloves assigning the value of $g(t,\theta)$ for a fixed θ to all of the points along $l(t,\theta)$. The summation of all of these back projections resembles the original function $f(\mathbf{x})$ with some smearing along the lines $l(t,\theta)$.

Thus, the reconstruction of a single small object would result in a star-like pattern. To counteract this smearing effect, slices of $g(t,\theta)$ for fixed θ are effectively filtered before the back projection operation (see figure 2.4). It will be shown later in this thesis that the object based reconstruction algorithm and the CBP method have a similar form with somewhat different interpretation.

2.3 Object Model

The first issue to address is the formulation of a model to represent objects. Let $K(\mathbf{c})$ denote a region of prescribed shape, size, and orientation centered around some point $\mathbf{c}\in\mathbb{R}^2$. That is, $K(\mathbf{c})$ is simply the object $K(0)$ translated so it is centered at $\mathbf{c}$. An object is represented by a function of the form

$$d\chi_{K(\mathbf{c})}(\mathbf{x})=d\chi_{K(0)}(\mathbf{x}-\mathbf{c})=df_o(\mathbf{x}-\mathbf{c}) \tag{2.9}$$

where d is the constant density of the object and χ is an indicator function defined as follows:

$$\chi_K(\mathbf{x})=\begin{cases} 1 & \text{if } \mathbf{x}\in K \\ 0 & \text{otherwise} \end{cases} \tag{2.10}$$

In order to allow us to include the possibility of estimating size, shape, and orientation, we can think of describing an individual object by $df_o(\mathbf{x}-\mathbf{c},\mathbf{v})$, where $\mathbf{c}$ is the location of the object's centroid and $\mathbf{v}$ is a vector containing the parameters specifying the object's geometry. Using this model, the total cross-sectional density $f(\mathbf{x})$ that we wish to consider can be represented by

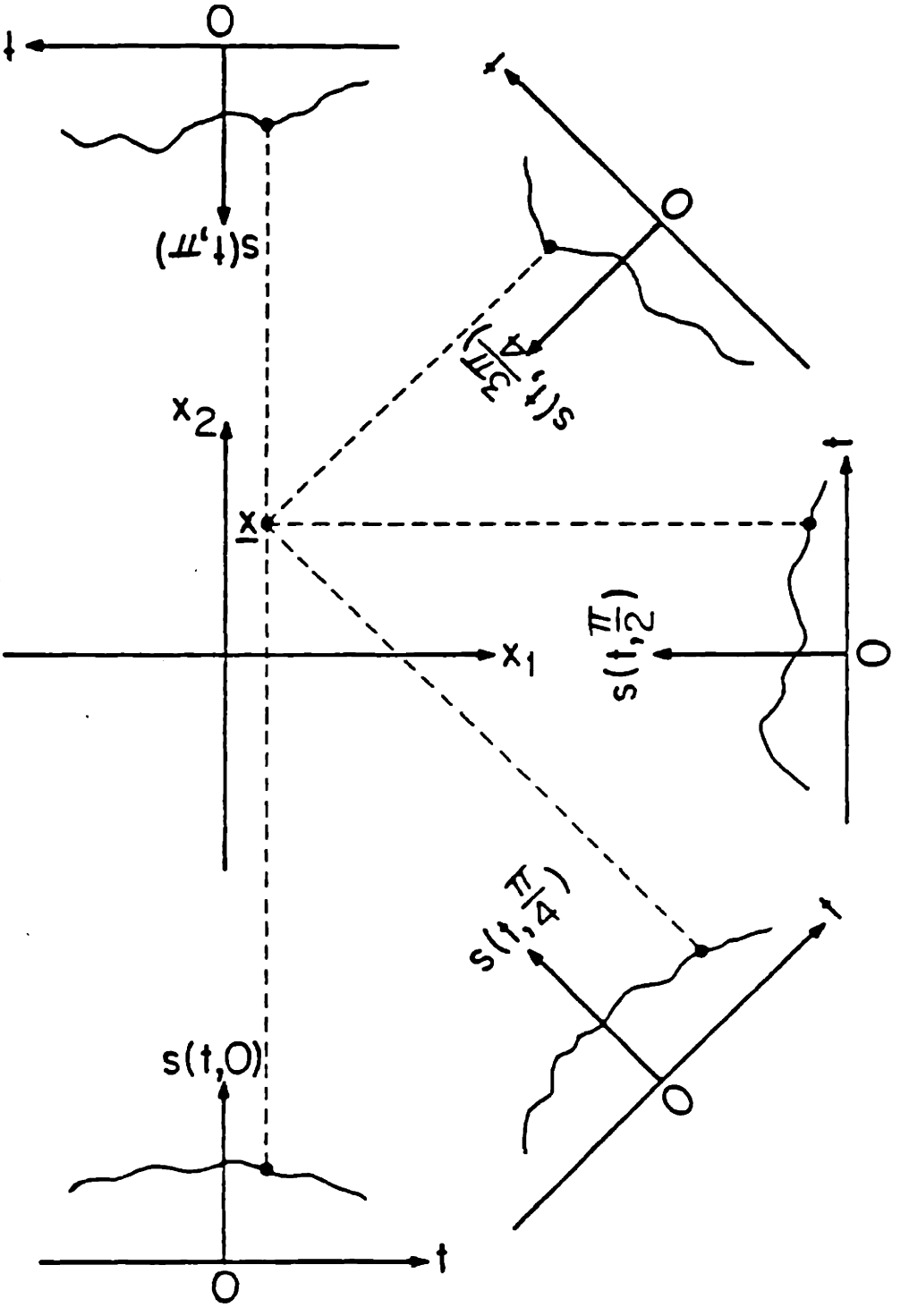

Figure 2-4: Back-projection operation.

some background field plus the superposition of N objects:

$$f(\mathbf{x})=f_b(\mathbf{x}) + \sum_{j=1}^{N} d_j f_o(\mathbf{x}-\mathbf{c}_j;\mathbf{v}_j) \tag{2.11}$$

Being independent of the $\mathbf{c}_j$'s and the $\mathbf{v}_j$'s and assumed known, $f_b(\mathbf{x})$ can be subtracted from $f(\mathbf{x})$ and effectively ignored in the object estimation problem. It is worth noting that it is not necessary for the background density to be constant but simply some known field.

For this thesis, the class of objects considered is restricted to the set of ellipses, but the ideas presented apply to more general objects. An ellipse can be viewed as the stretching and rotating of a circularly shaped object. Specifying a circular object, or a disc, is very simple.

$$df_o(\mathbf{x}-\mathbf{c};R)=\begin{cases} d & \text{if } \|\mathbf{x}-\mathbf{c}\|<R \\ 0 & \text{otherwise} \end{cases} \tag{2.12}$$

An ellipse can then be expressed as a transformation of this disc. Namely, let

$$\tilde{\mathbf{x}}\equiv Q(R,\lambda,\phi)\mathbf{x}=\begin{bmatrix} \cos\theta & \sin\theta \\ -\sin\theta & \cos\theta \end{bmatrix}\begin{bmatrix} \sqrt{\lambda} & 0 \\ 0 & 1/\sqrt{\lambda} \end{bmatrix}\begin{bmatrix} R & 0 \\ 0 & R \end{bmatrix}\mathbf{x} \tag{2.13}$$

Thus an ellipse of radius R, eccentricity λ, and orientation ϕ is just $f_o(Q^{-1}(R,\lambda,\phi)\mathbf{x};\mathbf{v})$. Restricting objects to be ellipses simplifies the problem to estimating the object's location and geometric parameters R, λ, ϕ.

2.4 Maximum Likelihood Parameter Estimation

In practice, the Radon transform of $f(\mathbf{x})$, $g(t,\theta)$, is not available. Rather, noisy measurements are taken. For sufficiently high X-ray doses in the case of CAT scans or acoustic energy in other applications, this noise can be modeled as Gaussian white noise. Thus, the actual data is in the form of:

$$y(t,\theta)=g(t,\theta)+w(t,\theta) \tag{2.14}$$

where $w(t,\theta)$ is a zero-mean Gaussian white noise process.

In this thesis we focus on the special case of (2.11) when there is only one object to be estimated (see chapter 5 when we consider what happens when there is a second object in the field).

In order to estimate an object's parameters a maximum likelihood approach is used. Maximum likelihood estimation can be explained as follows. Consider the conditional probability of some random variable x given a y, p(x|y). Given that we observe x, so that its value is known, we can think of p(x|y) as a function of y. The maximum likelihood estimate of y is the value of y that maximizes this likelihood function p(x|y). For the reconstruction problem, it is more convenient to work with the log of the likelihood function. This is valid because the point at which the peak of any likelihood function occurs is identical to the point at which the peak of the log of the function occurs. The log likelihood function, (Van Trees 1968), for our problem is given by:

$$L_{\Delta}(d,\mathbf{c},\mathbf{v})=2d\int_{\pi/2-\Delta}^{\pi/2+\Delta}\int_{-\infty}^{\infty}y(t,\theta)g(t,\theta;\mathbf{c},\mathbf{v})dtd\theta - d^2\int_{\pi/2-\Delta}^{\pi/2+\Delta}\int_{-\infty}^{\infty}g^2(t,\theta;\mathbf{c},\mathbf{v})dtd\theta \tag{2.15}$$

where 2Δ represents the total viewing angle (i.e. we observe $y(t,\theta)$ for $|\theta| \leq \Delta$), and $\Delta = \pi/2$ corresponds to the full view case. Since only discrete measurements are available, these integrals are approximated by sums.

The maximum likelihood estimates for the object's parameters are just the values of d, **c**, and **v** which maximize this function.

$$\begin{bmatrix} \hat{d} \\ \mathbf{c} \\ \mathbf{v} \end{bmatrix}_{ML} = \text{argmax} L_{\Delta}(d,\mathbf{c},\mathbf{v}). \tag{2.16}$$

For the cases considered in this thesis, the density of objects is considered to be known and can thus be ignored. The resulting problem focuses on the estimation of an object's location and geometry.

The log likelihood function (2.15) consists of two terms. The first term for each value of **v** is essentially the same as the CBP inversion formula (2.8) with the only difference being the kernel. In the log likelihood function, the kernel is not $V(\omega)=|\omega|$ but rather the Radon transform of the modeled object located at the origin. In this context, the kernel can simply be viewed as a matched filter. The likelihood function has its peak when the filter matches the data. The second term in the log likelihood function can be identified as the Radon tranform energy of the modeled object as a function of **c** and **v**.

It is important to point out that while the CBP inversion formula and the log likelihood function have similar forms, the use we make of it here is very different than that for standard reconstruction algorithms in which the kernel is chosen in order to achieve image clarity and quality. The log likelihood function's kernel is instead chosen to best estimate the object's parameters **c** and **v**.

In the next chapter, the behaviors of the log likelihood functions for the estimation of location, size, orientation, and eccentricity are examined separately. At the end of the chapter, an iterative algorithm using the estimates of location and geometry is described.

Chapter 3
An Iterative Algorithm for Object Estimation

The algorithm presented in this thesis has as components algorithms for the separate estimation of object location, size, orientation, and eccentricity. Starting with a coarse estimate of location, these parameters are estimated in an iterative fashion with the goal being to converge to a final best estimate of the actual object shape, size, and location. Thus, to obtain initial insight into the behavior of this algorithm, we begin by examining the nature and performance of the algorithms for the separate estimation of $\mathbf{c}$, R, ϕ, and λ.

3.1 Location Estimation

In this section, we address the problem of locating a single object having a known geometry. The maximum likelihood location estimate, $\mathbf{c}$, is obtained from the projection measurements by finding the value of $\mathbf{c}$ which maximizes $L_\Delta(\mathbf{c})$. Since $\mathbf{c}\in\mathbb{R}^2$, this involves locating the peak of the two-dimensional function given by:

$$L_\Delta(\mathbf{c})=2d\int_{\pi/2-\Delta}^{\pi/2+\Delta}\int_{-\infty}^{\infty} y(t,\theta))g(t,\theta;\mathbf{c},\mathbf{v})dtd\theta \qquad (3.1)$$
$$- d^2\int_{\pi/2-\Delta}^{\pi/2+\Delta}\int_{-\infty}^{\infty} g^2(t,\theta;\mathbf{c},\mathbf{v})dtd\theta$$

Equation 3.1 is essentially the same as (2.15). However, in this case, $\mathbf{v}$ and d are considered to be fixed; and the second term in (3.1), being the

Radon transform energy of the modeled object, can be shown to be constant when viewed as a function of $\mathbf{c}$ only. By a change of variables:

$$\int_{-\infty}^{\infty} g^2(t,\theta;\mathbf{c},\mathbf{v})dt = \int_{-\infty}^{\infty} g_o^2(t-\underline{\mathbf{c}}'\underline{\theta},\theta;\mathbf{v})dt \tag{3.2}$$

$$= \int_{-\infty}^{\infty} g_o^2(\tau,\theta;\mathbf{v})d\tau$$

where $\underline{\mathbf{c}}'\underline{\theta}=c_1\cos\theta+c_2\sin\theta$. Being independent of $\mathbf{c}$, this term is simply a constant which doesn't affect the location estimate and can therefore be omitted. Using the same notation as in (3.2) we see that the best estimate of $\mathbf{c}$ is the value which maximizes

$$L_\Delta(\mathbf{c}) = \int_{\pi/2-\Delta}^{\pi/2+\Delta} \int_{-\infty}^{\infty} y(t,\theta)g(t,\theta;\mathbf{c})dtd\theta \tag{3.3}$$

The effect of noise on this log likelihood function is shown by substituting $y(t,\theta) = g(t,\theta) + w(t,\theta)$ into 3.3.

$$L_\Delta(\mathbf{c}) = \int_{\pi/2-\Delta}^{\pi/2+\Delta} \int_{-\infty}^{\infty} g(\mathbf{c},\theta;\mathbf{c}_a)g(t,\theta;\mathbf{c})dtd\theta \tag{3.4}$$

$$+ \int_{\pi/2-\Delta}^{\pi/2+\Delta} \int_{-\infty}^{\infty} w(t,\theta)g(t,\theta;\mathbf{c})dtd\theta$$

$$\equiv \bar{a}_\Delta(\mathbf{c},\mathbf{c}_a) + n_\Delta(\mathbf{c})$$

where $\mathbf{c}_a$ corresponds to the actual objects location. The first term in this expression, $\bar{a}_\Delta$, is the expected value of the log likeihood function and is known as the *generalized ambiguity function* (Van Trees 1971). The second term gives the noise dependence of $L_\Delta(\mathbf{c})$.

For the computer simulations considered in this thesis, measurements where restricted to a maximum of 180 evenly spaced view angles θ, and 101 parallel lines of integration, or rays, for each view. For example, in a five

view case with 21 rays per view, measurements are generated at angles $\theta_j=j\pi/5$, j=0,1,...4 (i.e. 0, 36, 72, 108, and 144 degrees). The 21 parallel rays for each view, given by $t_m=5m$, m=-10,-9,...10 (i.e. an inter ray spacing of 5), are used to span the measurement space restricted to $|t|<50$. Thus, the log likelihood function for a disc of radius R=10 in the case described above is given by:

$$L(\mathbf{c})=\sum_{j=0}^{4}\sum_{m=-10}^{10} y(t_m,\theta_j)g(t_m-\mathbf{c}\theta_j,\theta) \tag{3.5}$$

$$\text{where } g(t)=\begin{cases}\sqrt{2R^2-t^2} & \text{if } |t|\leq R\\ 0 & \text{if } |t|>R\end{cases}$$

In order to generate the noisy projection measurements $y(t,\theta)$, pseudorandom Gaussian white noise having zero-mean and variance σ^2 is added to each of the line integrals. For all of the cases considered in this thesis, the signal-to-noise ratio (SNR) in decibels (dB) is defined as:

$$\text{SNR}=20\log\left\{\mathcal{E}_D/\sigma^2\right\} \tag{3.6}$$

where $\mathcal{E}_D$ is the Radon transform energy of the actual object. For the 5 view, 21 rays per view case

$$\mathcal{E}_D=\sum_{j=0}^{4}\sum_{m=-10}^{10} g^2(t_m,\theta_j) \tag{3.7}$$

Examining the figures 3.1 and 3.2, reveals the main features of the ambiguity function. The function has its peak at the true object location and approaches zero at angles far from the θ_j's. This star-like pattern is typical of the CBP algorithm used to generate the log likelihood function. However, it is

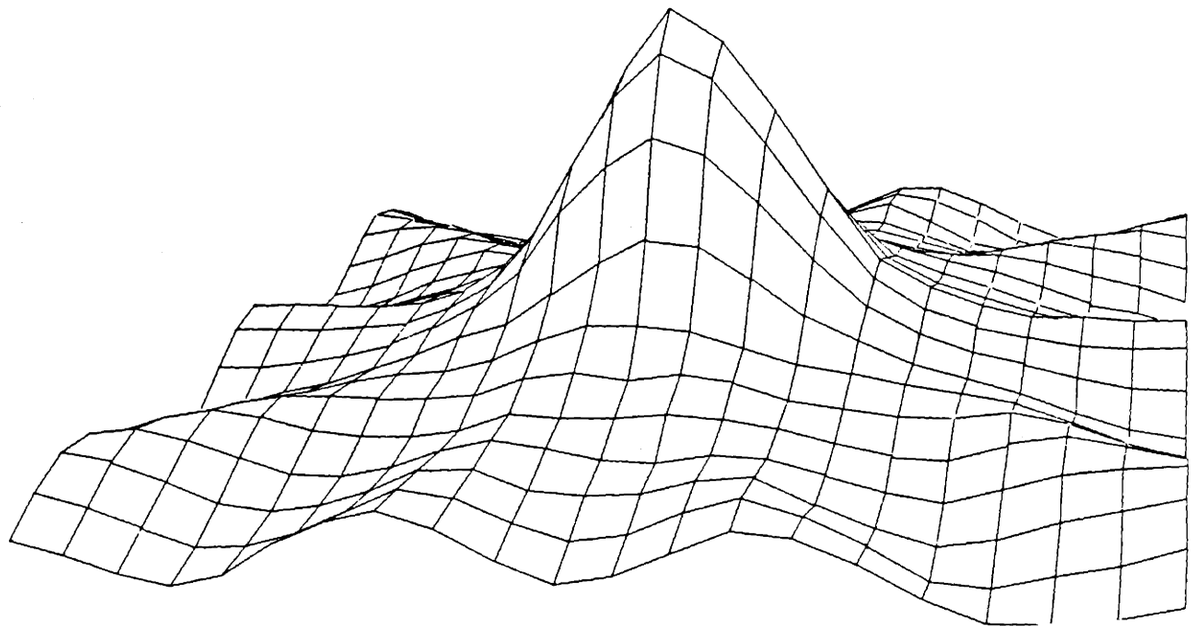

Figure 3-1: Five-view ambiguity function for disc of radius R=10 centered at the origin.

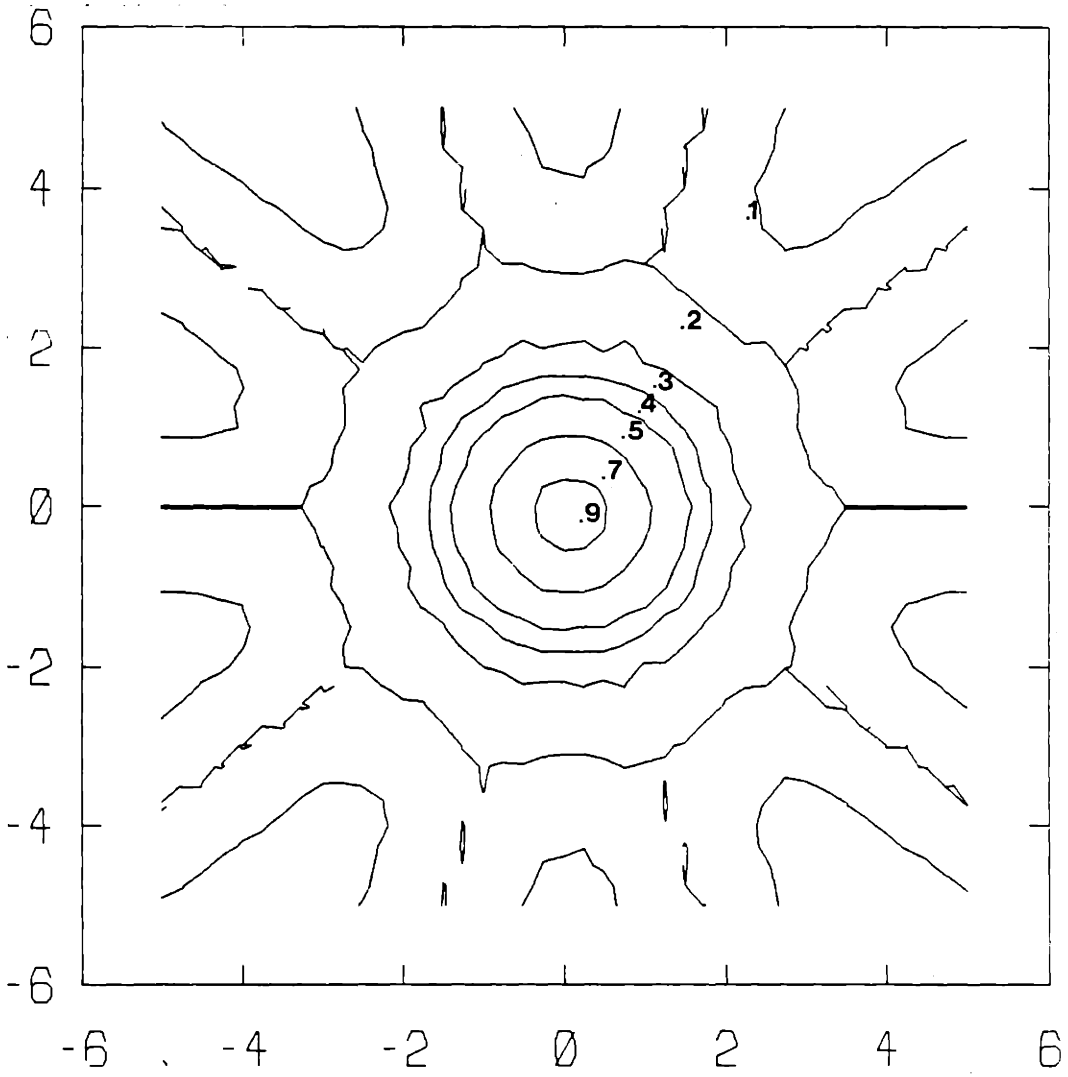

Figure 3-2: Contour plot of five-view ambiguity function for disc of radius R=10 centered at the origin

important to note that this function is optimized to peak at the true object location and is not intended to produce a clear picture of the original object. Performance is only measured by the location of the peak.

Rossi (1982) showed that the maximum likelihood estimate for the location of a single object is very robust to noise, limited data, and modeling errors. Working from the assumptions that the measurements could be modeled as smoothed projections corrupted by additive white noise and the cross-sectional field consisted of a single object of constant density superimposed on a known background field, Rossi showed that the maximum likelihood estimate of location using the log likelihood function is very accurate and reliable. Figure 3.3 is an example showing the log likelihood function of the same disk used in figures 3.1 and 3.2 with the addition of 0 dB of noise. The peak is at the actual object location of $\mathbf{c}$=(0.0,0.0).

In terms of modeling errors, Rossi showed that even with significant errors in R, ϕ, and λ for the modeled object the location estimate remains very near the true value. Performance was also shown to be relatively insensitive to the presence of other unmodeled objects that are smaller than approximately three-quarters of the size of the object to be located.

3.2 Size, Orientation, and Eccentricity Estimation

Unlike location estimation, the maximum likelihood estimates for size, orientation, and eccentricity only involve one-dimensional log likelihood functions. However, because the Radon transform energy of a modeled object for discrete cases is not independent of any of these geometric parameters, the second term in the log likelihood function, $L(\mathbf{v})$ must be retained.

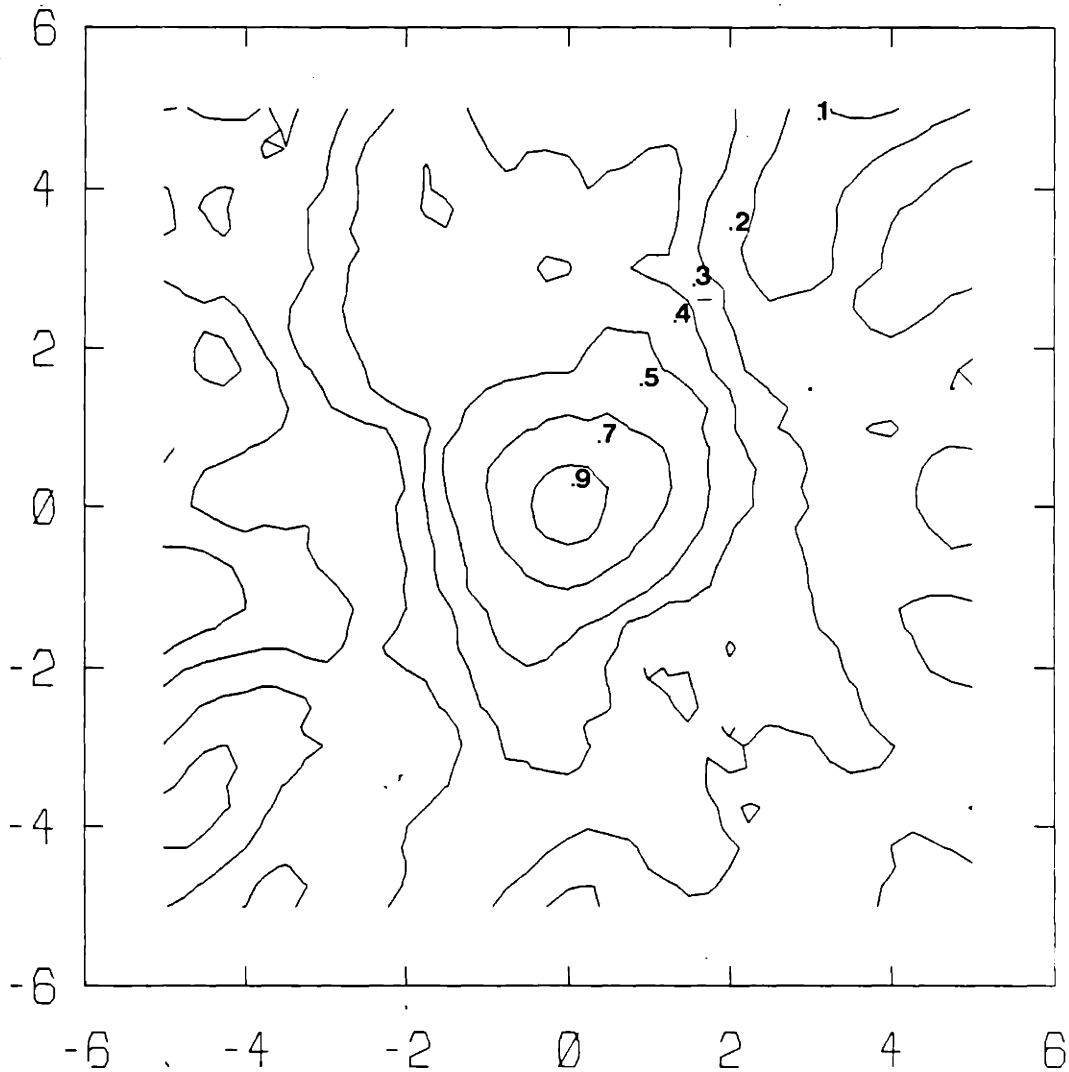

Figure 3-3: Contour plot of log likelihood function for disc at origin.

Information about these likelihood functions is most easily obtained by examing the shapes of the three ambiguity function curves (see figures 3.4, 3.5, and 3.6). Some observations about all three curves are immediately evident. First, the peaks are all unbiased, i.e. they all occur at the true value of the particular parameter being estimated. Performance in each case is solely dependent on the location and shape of this peak; the sharper the peak, the better the local error performance. Second, the absence of any side lobes indicates that the probability of any large errors is rather small.

The major issue that has to be addressed concerns how these curves change in the presence of modeling errors, limited data, and noise. The goal is to determine the reliability and accuracy of these estimates.

The robustness of the shapes of these curves (and hence the estimates derived from them) to modeling errors was examined by Rossi (1982). He showed that all of the curves are fairly robust to these type of errors. However, the eccentricity curve, being the flattest, achieved the worst performance. Concerning size estimation, Rossi found that an unbiased estimate cannot be obtained in the presence of errors in the modeled object's eccentricity. This is not surprising, since with an eccentricity error one is essentially trying to get the best approximation of an ellipse with one eccentricity in terms of a second ellipse with a different eccentricity. However, the magnitude of the bias in size estimation was a slowly increasing function of eccentricty, indicating that useful initial estimates can be obtained using a circularly-symmetric model. Furthermore, the orientation estimate was found to be unbiased in the presence of errors in modeled eccentricity, implying that the object orientation can be accurately estimated before the eccentricity is precisely known.

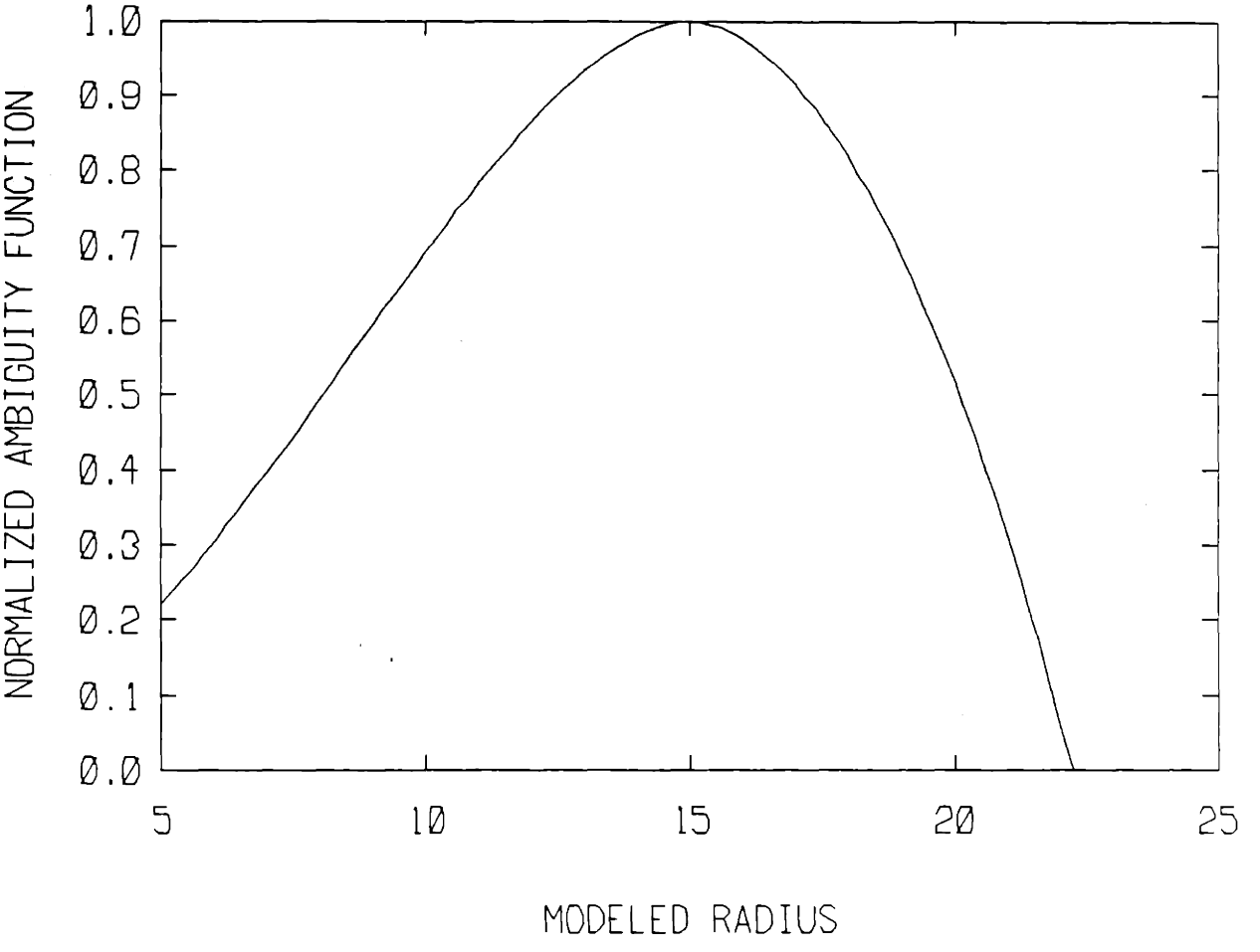

Figure 3-4: Size ambiguity function of ellipse (R=15, λ=4, ϕ=0) for 180 view, 101 rays per view, case.

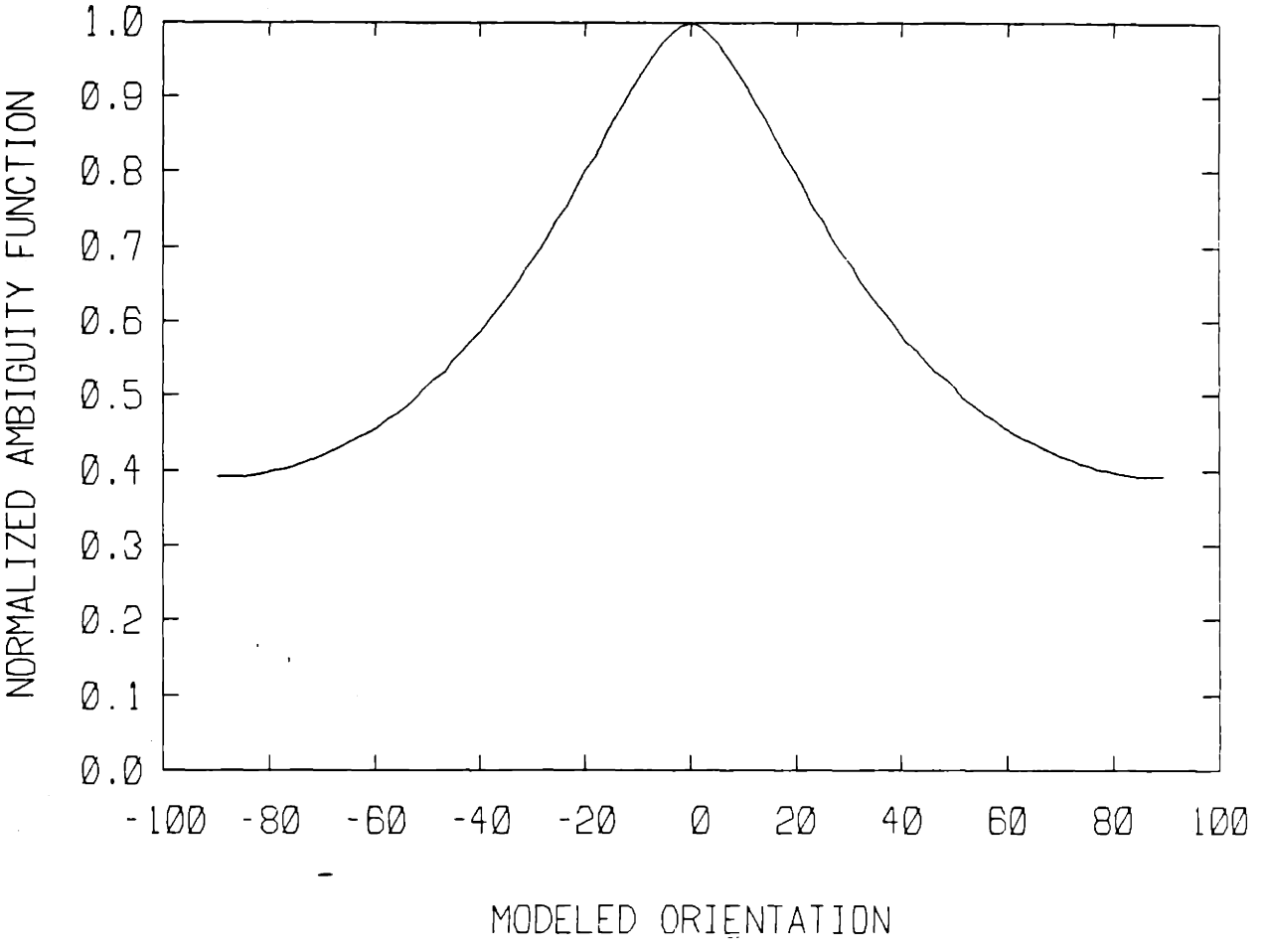

Figure 3-5: Orientation ambiguity function of ellipse (R=15, λ=4, ϕ=0) for 180 view, 101 rays per view, case.

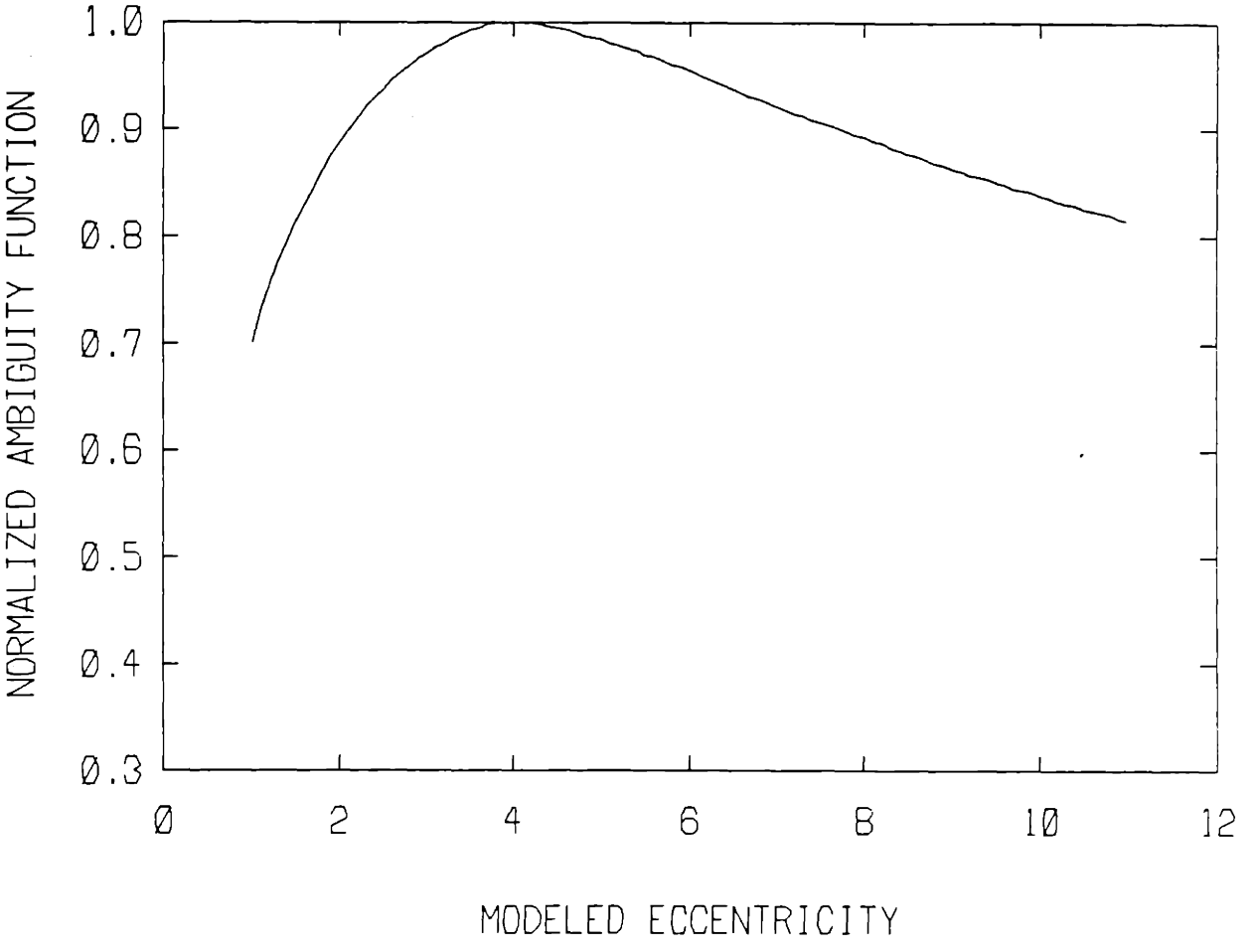

Figure 3-6: Eccentricity ambiguity function of ellipse (R=15, λ=4, ϕ=0) for 180 view, 101 rays per view, case.

The effect of the amount of available data on the estimation of these parameters is shown in figures 3.7, 3.8, and 3.9. The curves all get lower as the measurements become more and more sparse; however, the peaks are still unbiased.

The plots in figure 3.7 show that the log likelihood function for size estimation is very robust with respect to sparse data. The shapes of the curves change slightly, but the peaks retain the same essential shape. The eccentricity curves (see figure 3.9) are particularly flat, especialy when very few measurements are available. This implies that considerable data is necessary to accurately estimate object eccentricity, which is not surprising. The log likelihood function for orientation remain well behaved when more than five views are available. However, the curve basically breaks down at this point. Intuitively, in order to estimate orientation, measurements should be taken at many different angles.

In conclusion, the curves for size, orientation, and eccentricity estimation as a function of the amount of data essentially indicate that it is not necessary to take a large number of measurements. Performance doesn't seriously degrade until the number of views drops to well below twenty. Furthermore, the plots for the case of 45 views, 25 rays per view are very close to the case of 180 view, 101 rays per view. Therefore, in the computer simulations presented later in this thesis, the number of measurements generated is equal to or less than this particular case.

When noise is added to the data, the log likelihood functions retain the same general features present in the noise free case. Since performance is measured by the location of the peak, the lack of side lobes keeps the probability of gross errors small, even at high noise levels. Figures 3.10, 3.11,

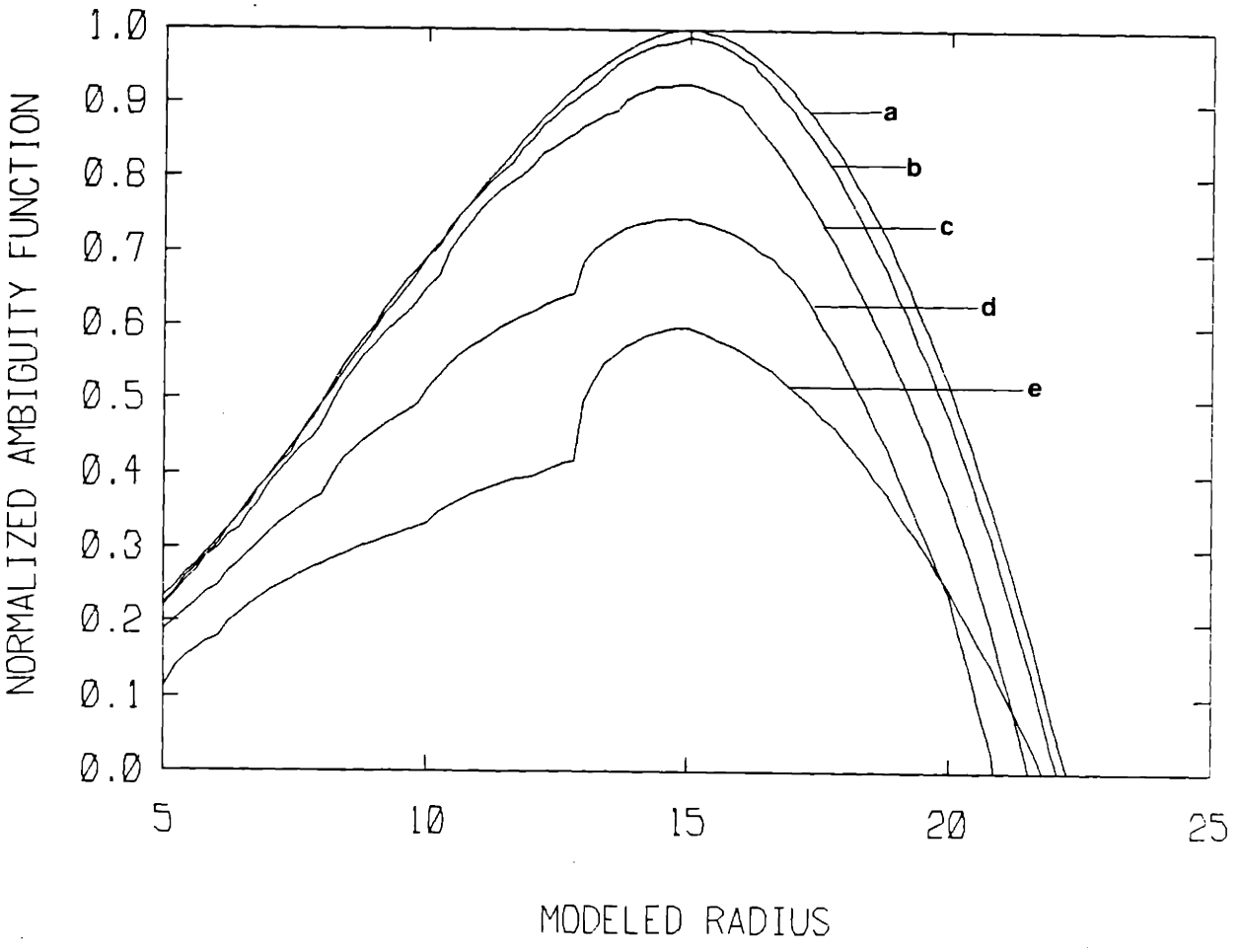

Figure 3-7: Size ambiguity function for ellipse (R=15, λ=4, ϕ=0) as a function of the amount of available data.

The number of measurements for the five curves shown are: a) 180 views 101 rays per view, b) 45 views 25 rays per view, c) 20 views 25 rays per view, d) 20 views 11 rays per view, e) 5 views 11 rays per view.

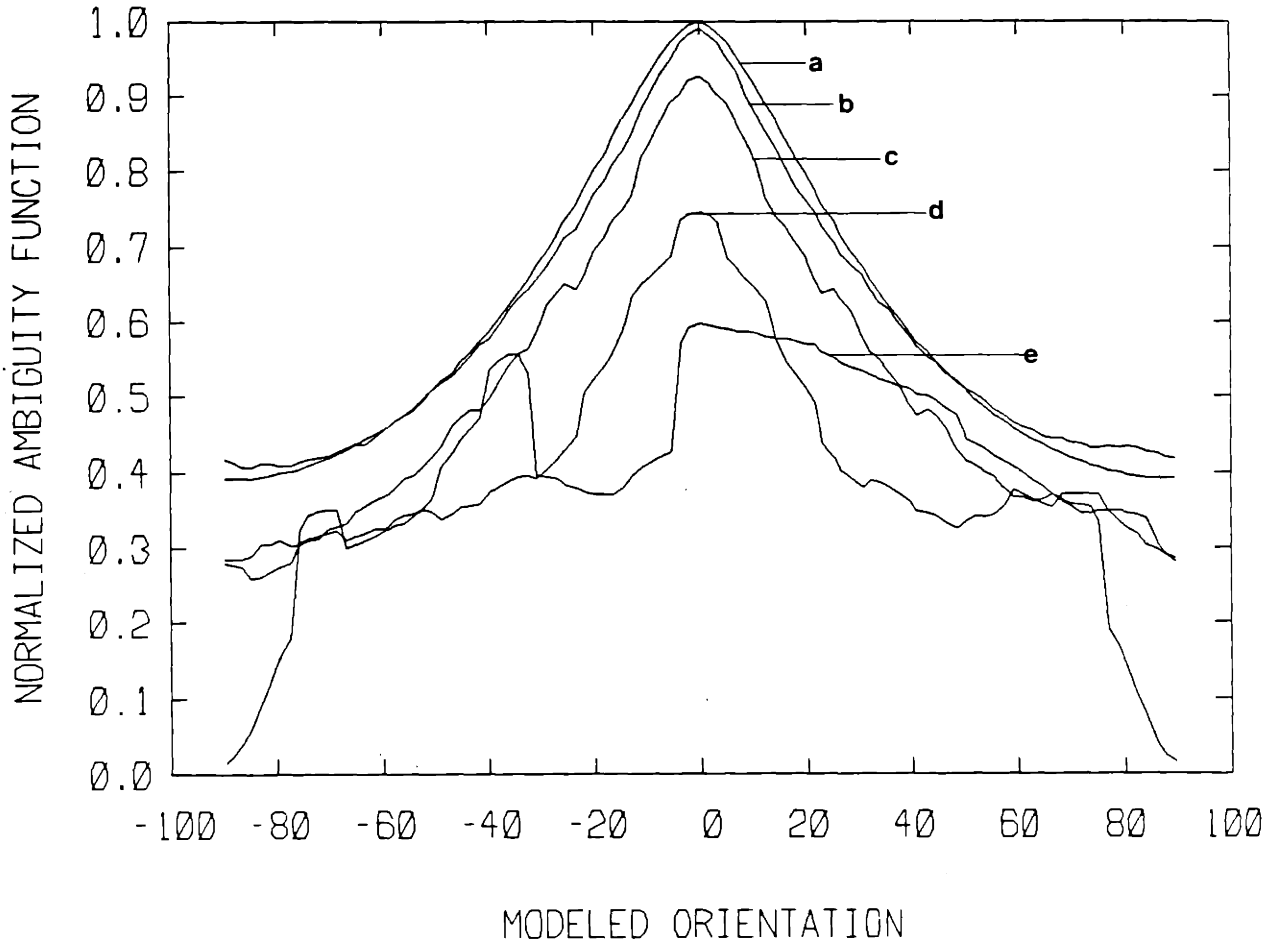

Figure 3-8: Orientation ambiguity function for ellipse (R=15, λ=4, ϕ=0) as a function of the amount of available data.

The number of measurements for the five curves shown are: a) 180 views 101 rays per view, b) 45 views 25 rays per view, c) 20 views 25 rays per view, d) 20 views 11 rays per view, e) 5 views 11 rays per view.

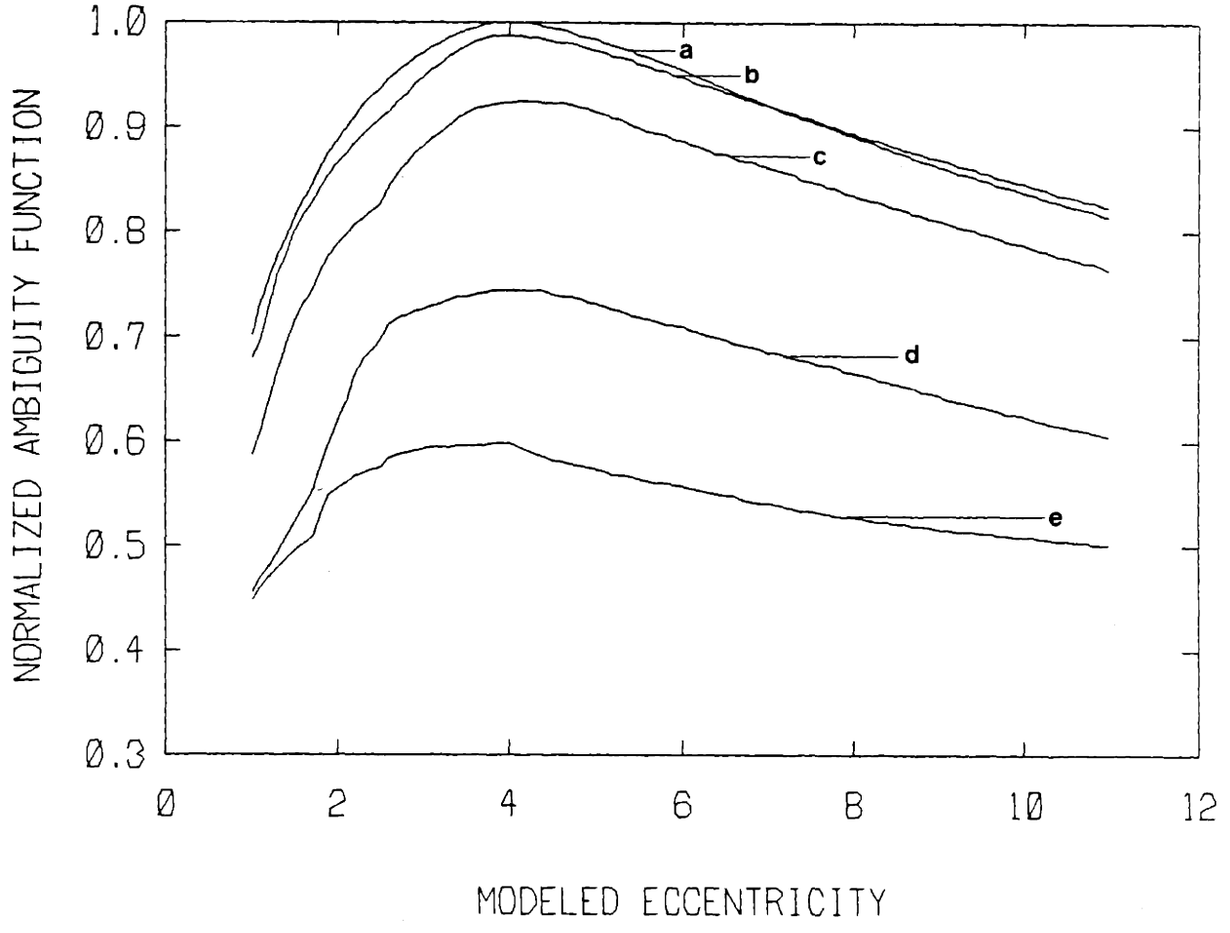

Figure 3-9: Eccentricity ambiguity function for ellipse (R=15, λ=4, ϕ=0) as a function of the amount of available data.

The number of measurements for the five curves shown are: a) 180 views 101 rays per view, b) 45 views 25 rays per view, c) 20 views 25 rays per view, d) 20 views 11 rays per view, e) 5 views 11 rays per view.

and 3.12 show a particular example of these likelihood functions with a SNR of 0 dB. The log likelihood function for the 180 view, 101 rays per view, case are practically unchanged by this amount of noise. This indicates that some smoothing and filtering is occurring. While the presence of noise in the case of 45 views and 25 rays per view is much more evident, the peaks of the curves are still close to the correct values. It is noteworthy that the largest error occurs in the estimation of eccentricity indicating that a comparatively high SNR is needed for an accurate estimate of this parameter.

3.3 An Iterative Estimation Algorithm

The robustness of the log likelihood functions to modeling errors, lack of data, and noise suggests the formulation of an iterative algorithm for estimating object location and shape. This algorithm was proposed by Rossi (1982).

A circularly-symmetric profile is used in the intial stages to determine coarse estimates of object location and size. The location estimate will be unbiased; however, the initial size estimate will be slightly off if the actual object is not circular. Orientation and eccentricity are next calculated based on the initial location and size estimates. Orientation is estimated first because it is unbiased in the presence of eccentricity modeling errors. In order to make the initial orientation estimation a nominal eccentricity of $\lambda=5$ is chosen. Eccentricity is then estimated using the now available estimates of location, size, and orientation. After eccentricity is estimated the process loops back to the top and re-estimates location, size, orientation, and eccentricity respectively. This recursive process continues until the values of $\hat{\mathbf{c}}$, $\hat{R}$, $\hat{\phi}$, and

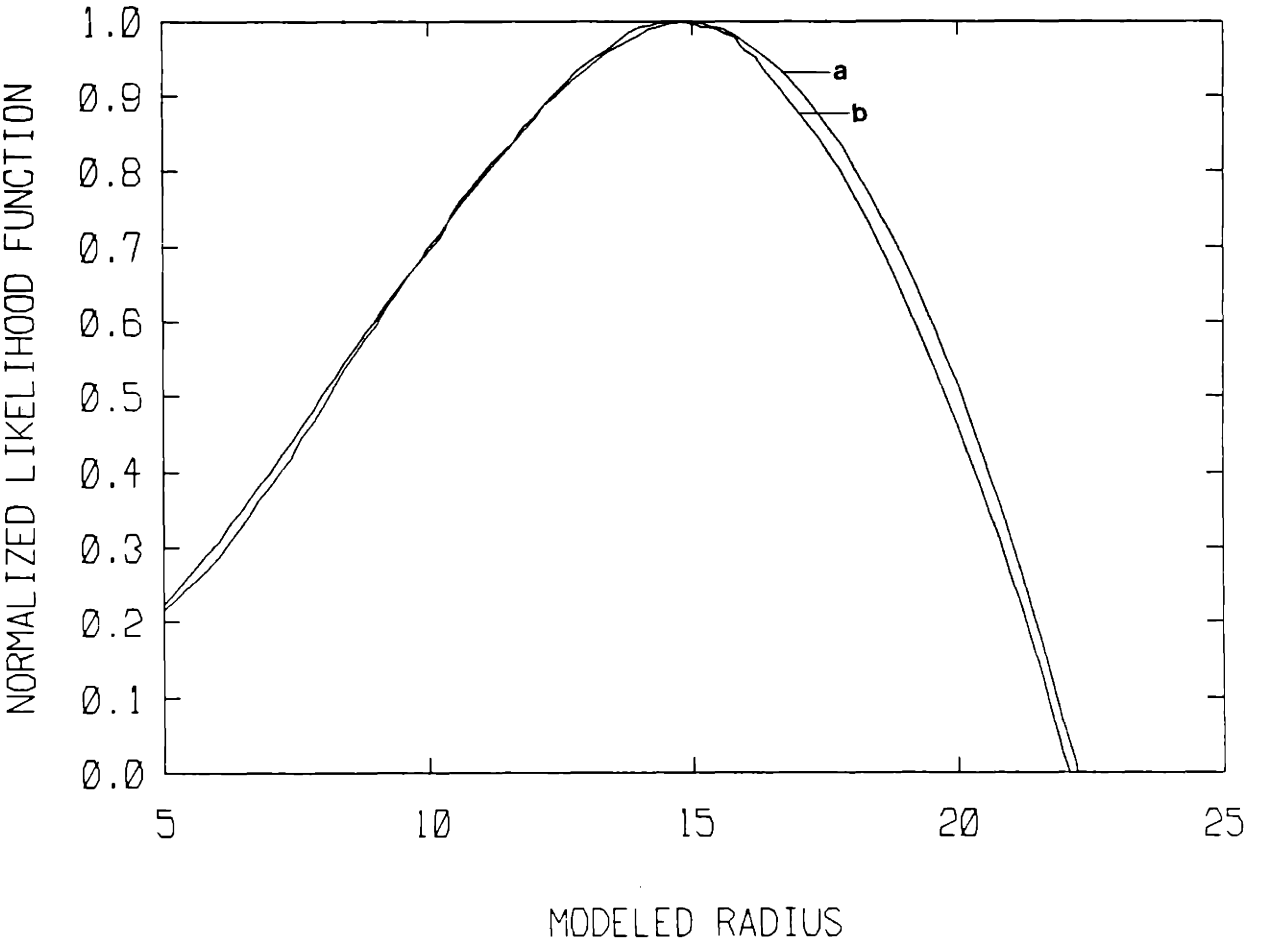

Figure 3-10: Size log likelihood function for ellipse (R=15, λ=4, ϕ=0) with the SNR=0dB.

The two curves shown correspond to: a) 180 view 101 rays per view case, peak at $\hat{R}$=14.8 b) 45 view 25 rays per view case, peak at $\hat{R}$=14.8.

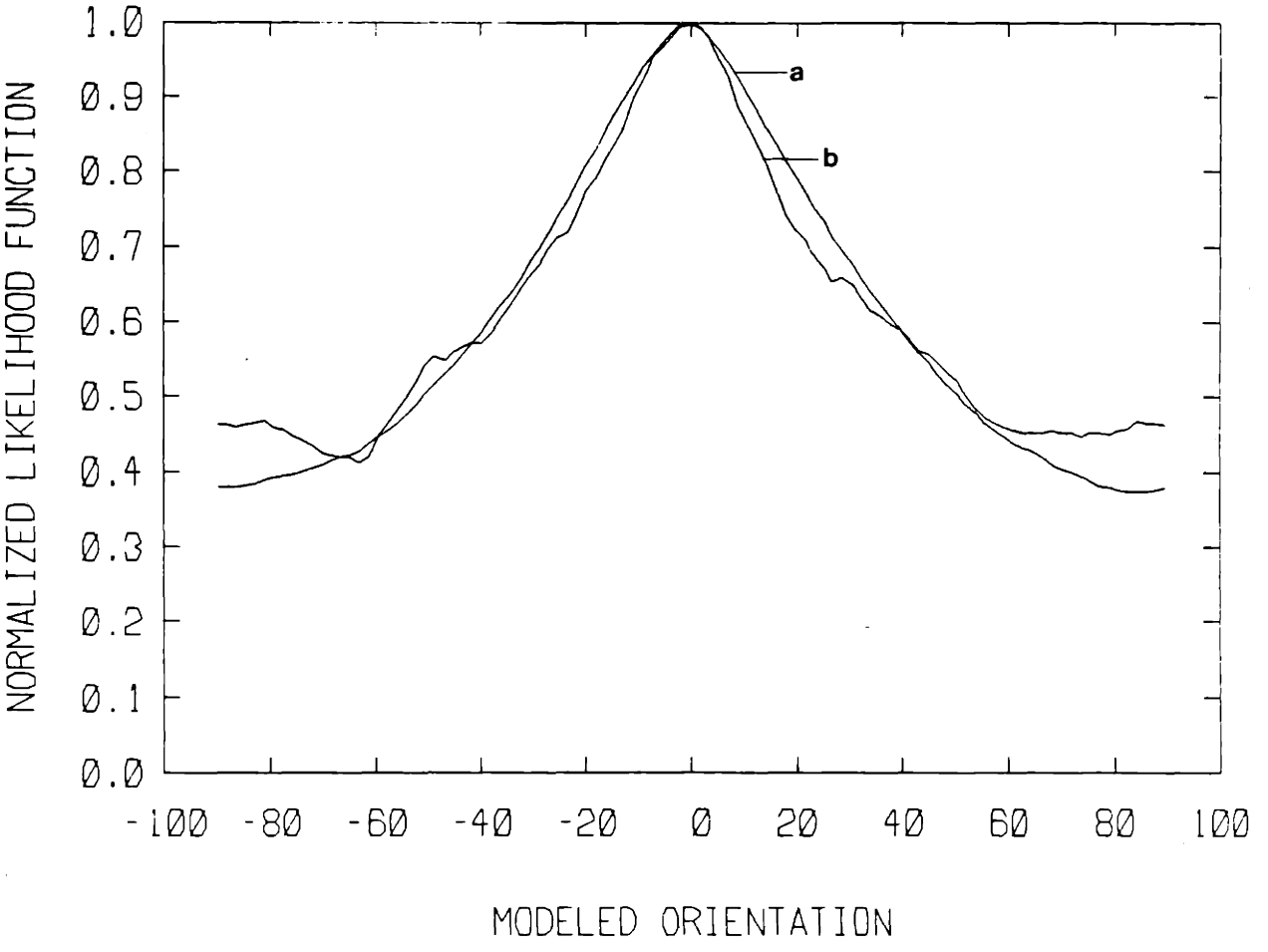

Figure 3-11: Orientation log likelihood function for ellipse (R=15, λ=4, ϕ=0) with the SNR=0dB.

The two curves shown correspond to: a) 180 view 101 rays per view case, peak at $\hat{\phi}$=0.0° b) 45 view 25 rays per view case, peak at $\hat{\phi}$=0.0°.

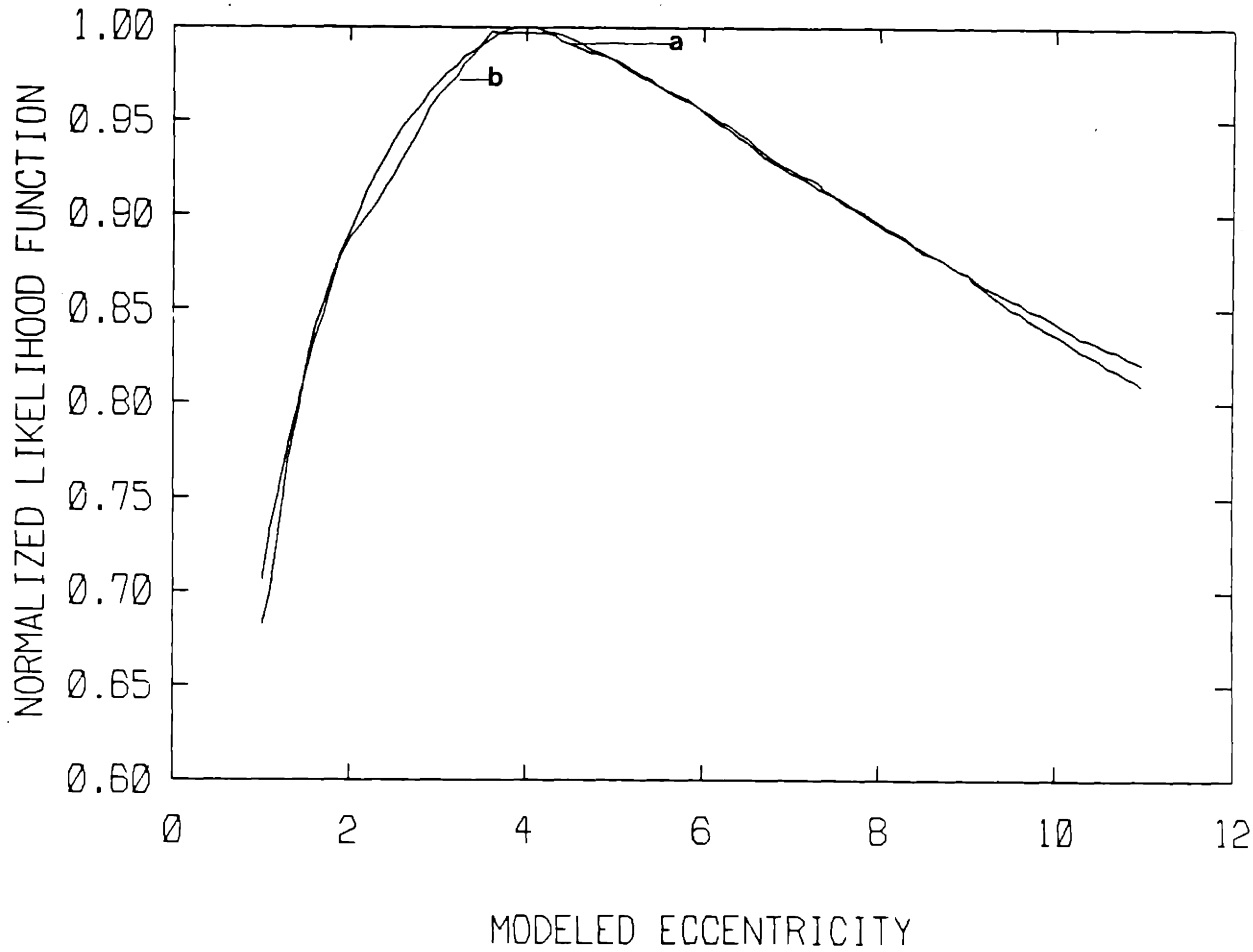

Figure 3-12: Eccentricity log likelihood function for ellipse (R=15, λ=4, ϕ=0) with the SNR=0dB.

The two curves shown correspond to: a) 180 view 101 rays per view case, peak at $\hat{\lambda}$=3.8 b) 45 view 25 rays per view case, peak at $\hat{\lambda}$=3.4.

$\hat{\lambda}$ remain unchanged for one complete iteration, where a complete iteration is defined here as the consecutive calculation of $\hat{\mathbf{c}}$, $\hat{R}$, $\hat{\phi}$, and $\hat{\lambda}$. After the best estimate for the object parameters have been found, one can consider looking for additional smaller objects. Figure 3.13 diagrams the total iterative algorithm.

For the computer simulations presented in this thesis, the parameters $\hat{\mathbf{c}}$, $\hat{R}$, $\hat{\phi}$, and $\hat{\lambda}$ were quantized. Thus, in most cases, absolute convergence was obtained in a finite number of steps. In problems with finer quantizations it might not be necessary to wait until absolute convergence. In fact, if these parameters are viewed as continuous, convergence is only asymptotic. Therefore, for these applications, some threshold for deciding when to stop must be used.

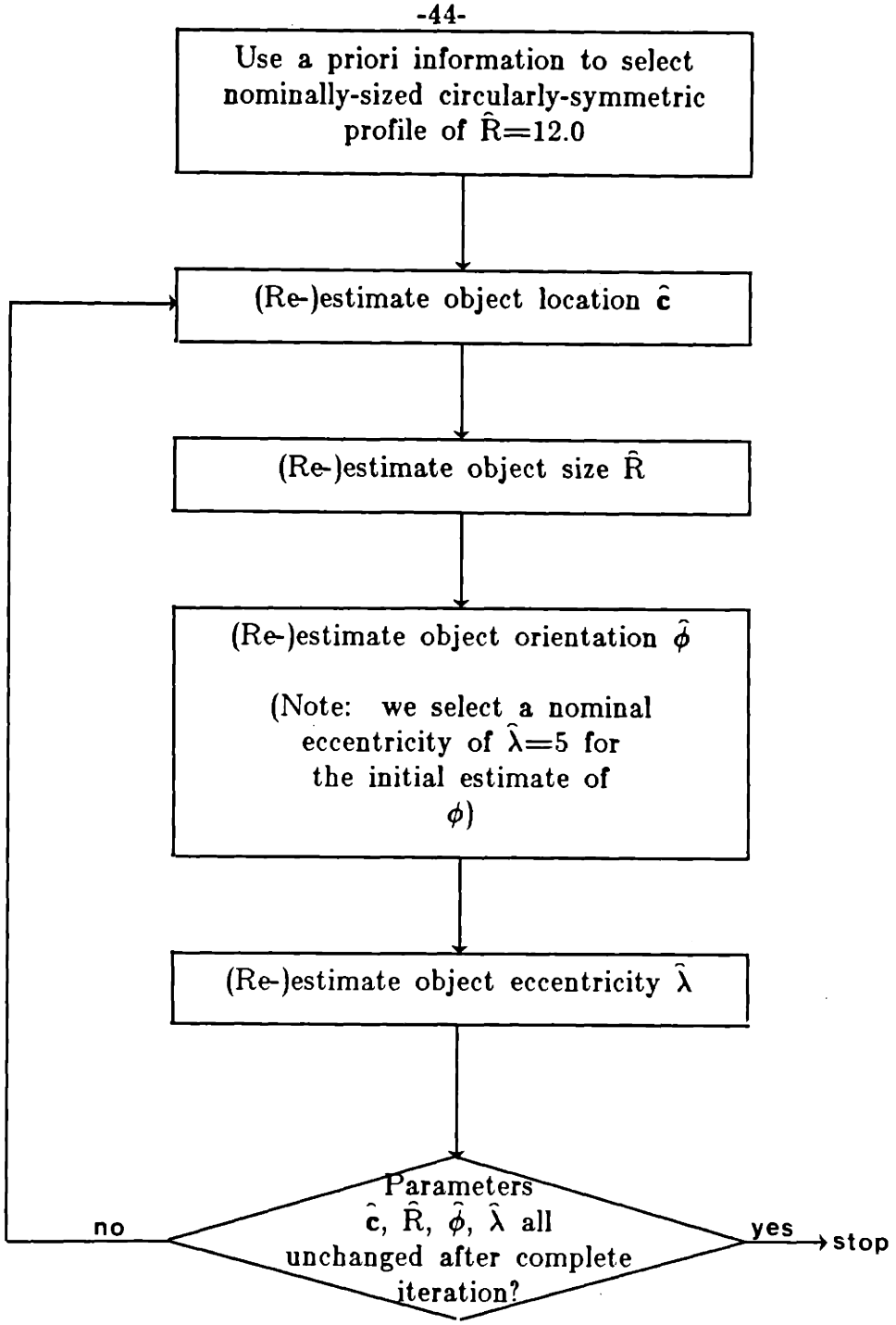

Figure 3-13: Block diagram for iterative single object estimation algorithm.

Chapter 4
Single Object Estimation

In this chapter we address the problem of detecting and estimating the geometry of a single object using the iterative algorithm previously described. The focus of this section is aimed at determining the accuracy and reliability of the algorithm. In particular, the robustness of this estimation technique to high noise levels, sparse data, and different object shapes is examined.

Computer simulations were used to analyze the performance of the iterative algorithm. Projection data for the particular object field being considered were generated and pseudorandom Gaussian white noise added to form the $y(t,\theta)$ in equation (2.14). The object location and geometric parameters were then estimated in an iterative fashion.

A detailed analysis of one example yields useful initial insight into the dynamics of the algorithm. The simulated density function, f(x), consisted of a single elliptical object located at the origin having radius R=10, orientation ϕ=0, and eccentricity λ=9. Noise was added to the projection data that consisted of 45 evenly spaced views with 25 rays per view. The signal-to-noise ratio was 0dB.

Location was first estimated using an initial model of a disc of radius 12. Despite the fact that the modeled circular shape was dramatically different than the shape of the actual object, the initial location estimate was $\mathbf{c}$=(-2.53,0.42), which is quite accurate. Size was estimated next, still using the disk-shaped model but now assuming the estimated location was the actual

location. After estimating orientation (using an assumed eccentricity of $\lambda=5$) and eccentricity (using the orientation estimate just determined), the algorithm loops back to the top and reestimates location. This process continues until convergence occurs (see table 4-I for the results of this simulation).

Table 4-I shows that the algorithm rapidly converges to an estimate very close to the actual object. Since the estimated parameters are used as inputs for the next iteration, once a complete iteration is performed without any changes in the parameter values, further calculations will not alter the model. Since we have quantized these parameters, this typically happens in a few iterations (see section 5.1 for a discussion of an example where an oscillation due to this quantization occurs).

While the final answer is reached within three complete iterations in this case, after the first iteration, the algorithm essentially engaged in "fine tuning" the final estimate. The initial estimated parameters are fairly accurate, and further calculations are small adjustments of these values. Figure 4.1 shows this more clearly. This rapid convergenee, basically indicates that the overall algorithm is very robust to the nominal model chosen for the initial estimates.

The same general behavior was observed in all of the other simulations performed for this chapter. Within one or two complete iterations, a reasonably accurate model of the true object was obtained; further iterations served to refine this initial estimate. In the remaining sections of this chapter, we systematically explore the accuracy and limitations of this single object estimation technique through a variety of computer simulations.

iteration #	object model				ML estimate
	$\hat{\mathbf{c}}$	$\hat{R}$	$\hat{\phi}$	$\hat{\lambda}$	
1	-	12.0	-	1.0	$\mathbf{c}$=(-2.52,0.42)
	(-2.52,0.42)	-	-	1.0	R=7.8
	(-2.52,0.42)	7.8	-	5.0	ϕ=0.0
	(-2.52,0.42)	7.8	0.0	-	λ=10.7
2	-	7.8	0.0	10.7	$\mathbf{c}$=(1.26,0.0)
	(1.26,0.0)	-	0.0	10.7	R=10.0
	(1.26,0.0)	10.0	-	10.7	ϕ=0.0
	(1.26,0.0)	10.0	0.0	-	λ=8.6
3	-	10.0	0.0	8.6	$\mathbf{c}$=(0.0,0.0)
	(0.0,0.0)	-	0.0	8.6	R=10.0
	(0.0,0.0)	10.0	-	8.6	ϕ=0.0
	(0.0,0.0)	10.0	0.0	-	λ=9.3
4	-	10.0	0.0	9.3	$\mathbf{c}$=(0.0,0.0)
	(0.0,0.0)	-	0.0	9.3	R=10.0
	(0.0,0.0)	10.0	-	9.3	ϕ=0.0
	(0.0,0.0)	10.0	0.0	-	λ=9.3

Table 4-I: Individual steps in the estimate of an ellipse ($\mathbf{c}$=(0,0), R=10, ϕ=0, λ=9) with SNR=0dB.

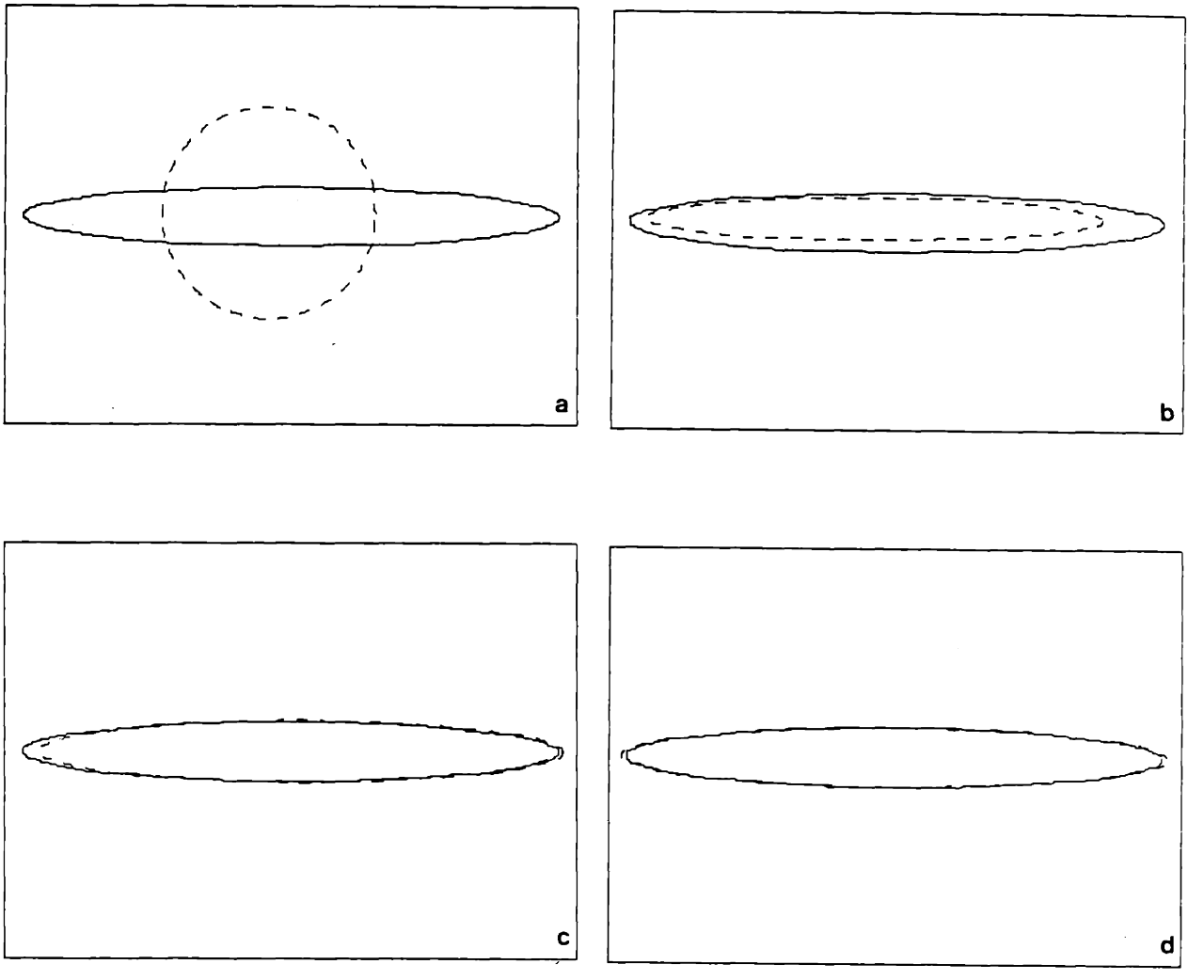

Figure 4-1: Intermediate steps for the estimation of an ellipse ($\mathbf{c}$=(0,0), R=10, λ=9, ϕ=0) with the SNR=0dB.

The solid line represents the actual ellipse; the dashed line is the estimated model. The four plots correspond to: a) initial estimate $\hat{\mathbf{c}}$=(-2.52,0.42), $\hat{R}$=12.0, $\hat{\lambda}$=1.0 b) after one complete iteration $\hat{\mathbf{c}}$=(-2.52,0.42), $\hat{R}$=7.8, $\hat{\lambda}$=10.7, $\hat{\phi}$=0.0° c) after two iterations $\hat{\mathbf{c}}$=(1.26,0.0), $\hat{R}$=10.0, $\hat{\lambda}$=8.6, $\hat{\phi}$=0.0° d) third and final estimate $\hat{\mathbf{c}}$=(0.0,0.0), $\hat{R}$=10.0, $\hat{\lambda}$=9.3, $\hat{\phi}$=0.0°.

4.1 Robustness to Measurement Noise

As more and more noise is added to the projection measurements, the performance of the iterative algorithm naturally degrades somewhat. It is instructive to understand how performance is affected by the noise, and to determine the limits -- in terms of signal-to-noise ratio and the amount of data -- below which the estimate's accuracy is severely degraded.

Several computer simulations were performed using noise of various levels of intensity superimposed on a density field consisting of a single ellipse centered at the origin with radius R=10, orientation ϕ=0, and eccentricity λ=9. Data were generated for the 45 view 25 rays per view case.

In the noise-free case (i.e. SNR=∞) the algorithm converges exactly to the actual object at the end of three complete iterations. Moreover, at moderate to high noise levels, the iterative algorithm's final estimates were found to be very robust to the presence of noise. Figure 4.2 shows the results for four different SNR's.

With a SNR of 0dB (i.e. a noise variance to signal energy ratio of one) the only final error was a 3% error in the eccentricity estimate. Even for the case of the SNR=-17.4dB, corresponding to a noise variance of almost eight times the signal energy, the final estimates remained very close to the true object parameter values.

Noticable degradation of performance occurred at a SNR of -26dB. Even at this very high noise level the algorithm was still, however, able to accurately estimate location and size. The final location and size estimates were $\hat{\mathbf{c}}$=(-0.84,-0.84) and $\hat{\mathrm{R}}$=10.4 respectively. This implies that these estimates are more robust that those for orientation and eccentricity, as

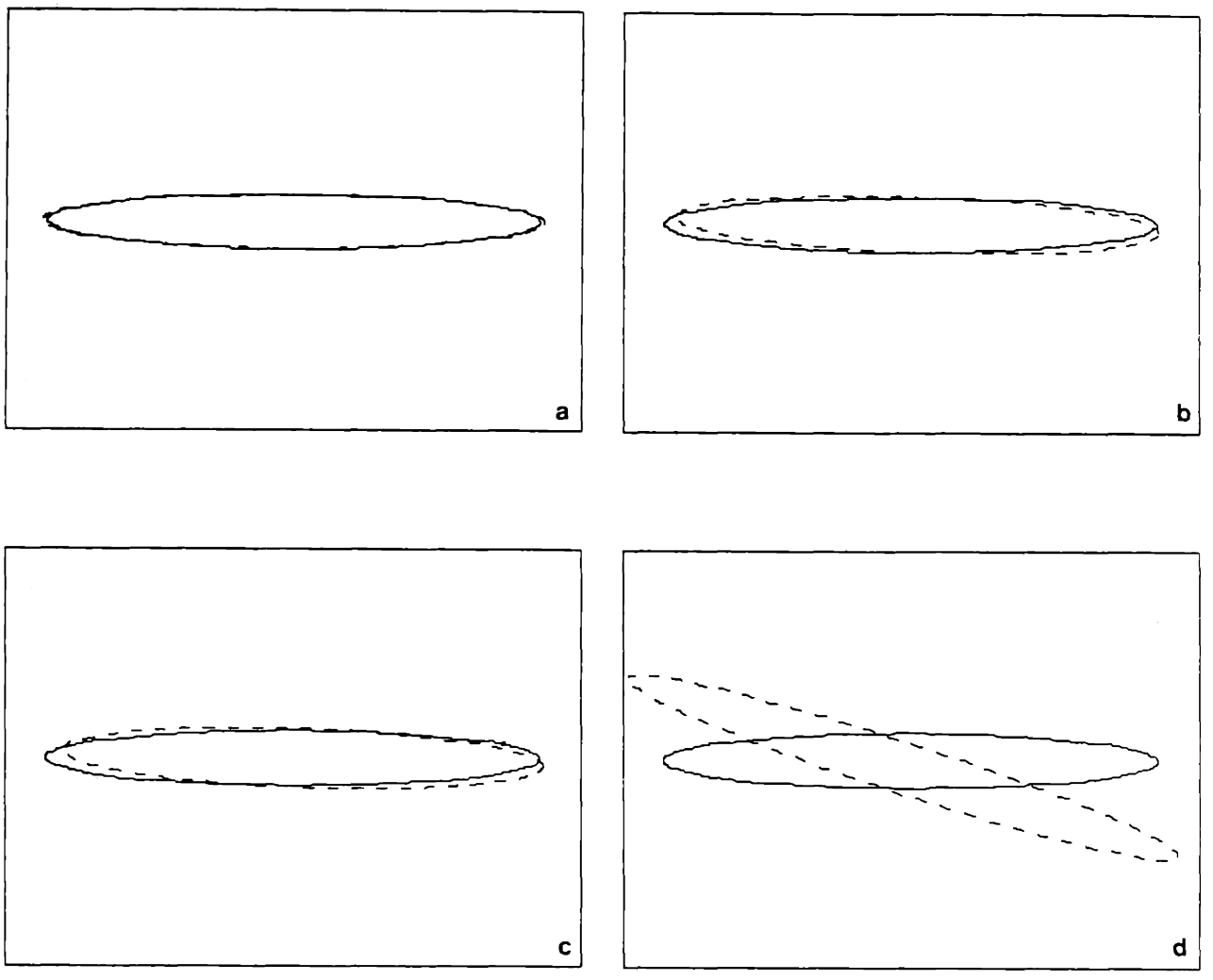

Figure 4-2: Estimation results for an ellipse (R=10, λ=9, ϕ=0) with four SNR's.

The actual object (solid line) is centered at the origin. The four cases shown correspond to: a) SNR=0dB, estimate is $\hat{\mathbf{c}}$=(0.0,0.0), $\hat{R}$=10.0, $\hat{\lambda}$=9.3, $\hat{\phi}$=0.0° b) SNR=-8.7dB, estimate is $\hat{\mathbf{c}}$=(0.84,0.0), $\hat{R}$=10.0, $\hat{\lambda}$=8.6, $\hat{\phi}$=-1.8° c) SNR=-17.4dB, estimate is $\hat{\mathbf{c}}$=(1.26,0.0), $\hat{R}$=10.2, λ=8.2, ϕ=-1.8° d) SNR=-26.1dB, estimate is $\hat{\mathbf{c}}$=(-0.84,-0.84), $\hat{R}$=10.4, $\hat{\lambda}$=11.4, $\hat{\phi}$=-18.0°.

predicted by Rossi.

For most applications, the SNR is considerably higher than -17.4dB. These simulations, therefore, show that for such applications this iterative algorithm is very accurate and reliable. When only extremely noisy data is available, location and size estimates are more reliable than the estimates of orientation and eccentricity.

4.2 Robustness to Object Shape

Orientation estimates for highly eccentric objects are very accurate. Estimating the orientation of an almost circular object is, however, considerably more difficult. Thus, very eccentric objects should be easier to estimate; and, in this section, we explore the reliablity of the iterative algorithm as the object being estimated becomes progressively more circular.

Data were generated for four cases. The density field for each 45 view 25 rays per view case consisted of a single ellipse centered at the origin with a radius R=10 and orientation ϕ=0. Noise at a level leading to a SNR of 0dB, was added to the generated data. The values for eccentricity used in the four cases were λ=9, 6, 3, and 1 respectively (see figure 4.3). Note that in the final case, λ=1, the object is actually a disc.

As expected, the best performance was achieved in the most eccentric case. However, the performance was not seriously affected as the eccentricity decreased.

Errors for this type of object estimation can be measured by the area of the actual object which is not enclosed by the estimated model and the area

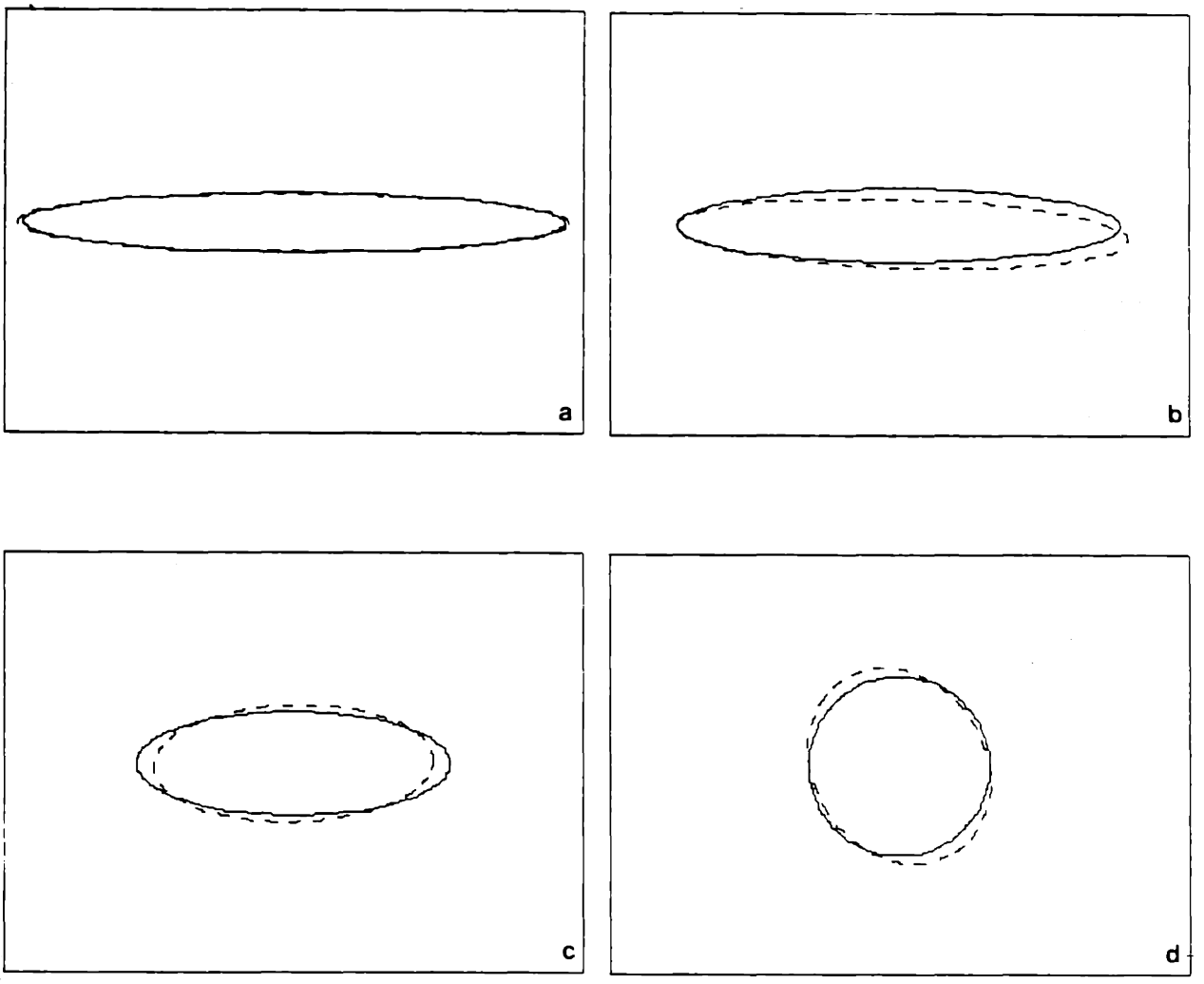

Figure 4-3: Estimation results for ellipses (R=10 ϕ=0) with eccentricities λ=9, 6, 3, 1 respectively.

The SNR=0dB and the final estimates (dashed lines) were: a) $\dot{\mathbf{c}}$=(0.0,0.0), $\dot{R}$=10.0, $\dot{\lambda}$=9.3, $\dot{\phi}$=0.0 b) $\dot{\mathbf{c}}$=(0.42,-0.84), $\dot{R}$=9.8, $\dot{\lambda}$=6.5, $\dot{\phi}$=-1.8° c) $\dot{\mathbf{c}}$=(0.0,0.0), $\dot{R}$=10.0, $\dot{\lambda}$=2.4, $\dot{\phi}$=1.8° d) $\dot{\mathbf{c}}$=(0.0,0.0), $\dot{R}$=10.4, $\dot{\lambda}$=1.2, $\dot{\phi}$=-57.6°.

of the estimated model which is outside of the actual object. Thus, for these simulations, even with a moderately low SNR of 0dB, the final estimates for all four cases were reasonably accurate and converged after an average of three complete iterations. For example, in the λ=1 case, the final estimate was $\hat{\mathbf{c}}$=(0,0), $\hat{R}$=10.4, $\hat{\lambda}$=1.2, and $\hat{\phi}$=-57.6°. These simulations indicate that this algorithm is reliable for estimating ellipses of various eccentricities but is the most accurate for highly eccentric cases.

4.3 Robustness to Limited Data

One of the prime motivations for developing an object-based reconstruction technique was to achieve performance, using less data, equal to or better than conventional methods. Thus, in this section, we examine important issues concerning performance when relatively few measurements are available. We consider two situations: evenly spaced but sparse measurements and measurements spanning a limited viewing angle (i.e. $\Delta<\pi/2$ in equation (2.15)). The limited view case is important for those applications in which data cannot be taken over the full range $0<\theta<\pi$.

Figure 4.4 shows the results of four simulations again using an ellipse centered at the origin (R=10, ϕ=0, λ=9). Gaussian white noise at a SNR of 0dB was added to the data for the four cases consisting of 45 views 11 rays per view, 20 views 25 rays per view, 20 views 11 rays per view, and 5 views 11 rays per view. While performance degrades as fewer measurements are available, the results remain accurate until the case using only 55 measurement points (5 views and 11 rays per view). For this extreme case, the final estimates of location and size are still fairly accurate, $\hat{\mathbf{c}}$=(-2.10,-0.42) and

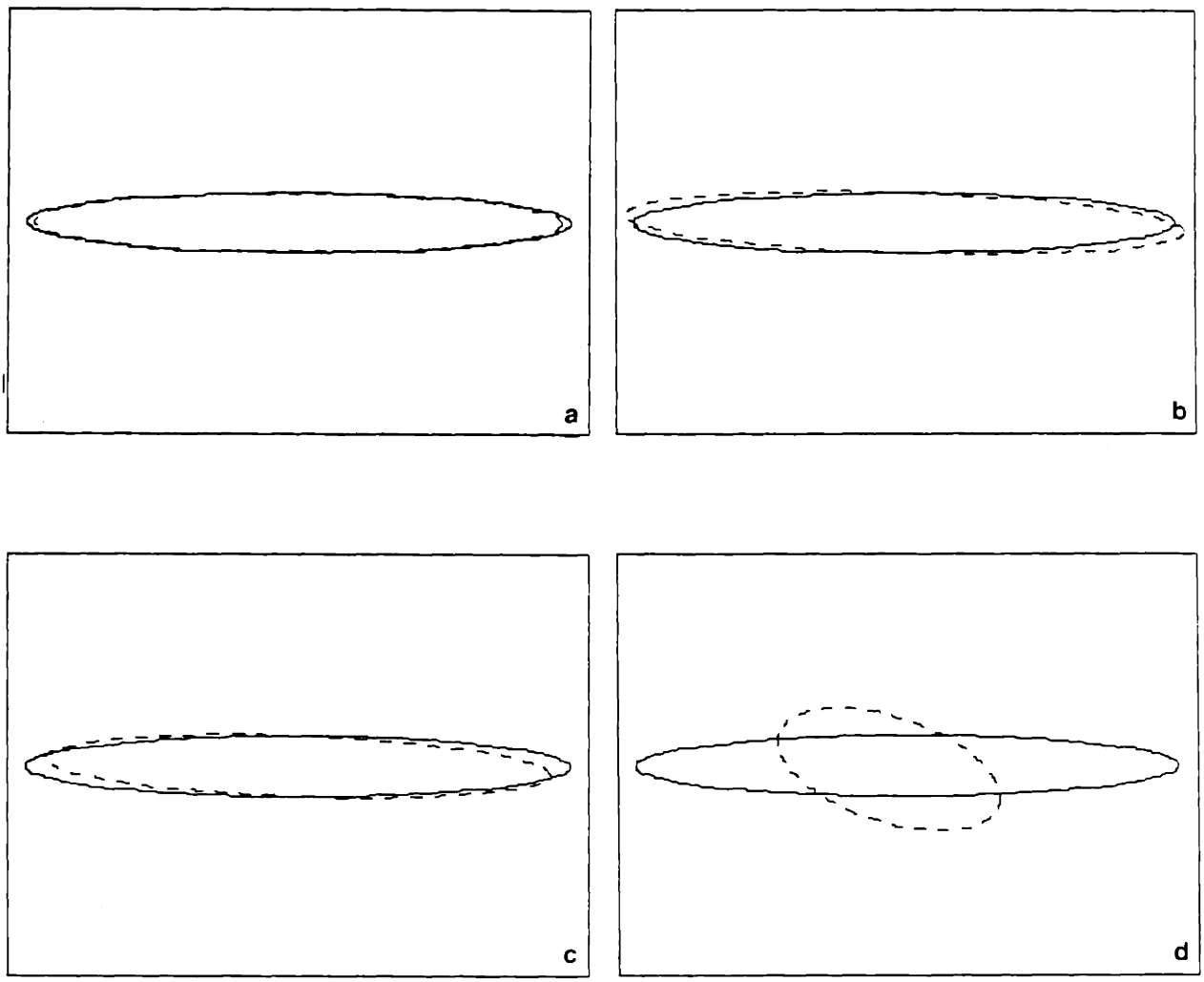

Figure 4-4: Estimation results for ellipse (R=10, λ=9, ϕ=0) using 45 view 11 rays per view, 20 views 25 rays per view, 20 views 11 rays per view, and 5 views 11 rays per view respectively

The SNR was 0dB, and the final estimates were: a)$\hat{\mathbf{c}}$=(0.0,0.0), $\hat{R}$=9.8, $\hat{\lambda}$=8.8, $\hat{\phi}$=0.0° b) $\hat{\mathbf{c}}$=(0.0,0.0), $\hat{R}$=10.2, $\hat{\lambda}$=9.2, $\hat{\phi}$=-1.8° c) $\hat{\mathbf{c}}$=(0.0,0.0), $\hat{R}$=9.6, $\hat{\lambda}$=8.4, $\hat{\phi}$=1.8° d) $\hat{\mathbf{c}}$=(-2.10,-0.42), $\hat{R}$=8.6, $\hat{\lambda}$=2.2, $\hat{\phi}$=-18.0°

$\hat{R}$=8.6. This implies a conclusion similar to that found in the high noise simulations; namely when very sparse measurements are available, orientation and eccentricity estimates cannot be considered reliable. For such cases, it makes sense to model all objects as being circularly symmetric.

The limited view cases presented in this thesis used a viewing angle resticted to 60 degrees, $\pi/3<\theta<2\pi/3$. We first considered a field consisting of the same ellipse previously used (**c**=(0,0), R=10, λ=9) with 0dB of noise. Three simulations were performed with the ellipse orientated at ϕ=0, $\phi=\pi/4$, and $\phi=\pi/2$ (see figure 4.5). In each case, measurements for 31 views and 25 rays were used to span the 60 degree viewing angle.

Two cases, ϕ=0 and $\phi=\pi/4$, yielded very accurate results. The final estimates for the third case, where the major axis of the ellipse was oriented along the same direction as most of the measurement rays, were, however, highly inaccurate. The algorithm was simply unable to estimate this ellipse since it was provided with little "broadside" information. When the noise level was reduced to 8.7 dB, a much closer estimate of the true object in the $\phi=\pi/2$ case was obtained (see figure 4.5d). These results support the conclusion that the best performance is obtained when measurements are taken along lines perpendicular to the major axis of an elongated object.

Computer simulations were also performed for the same limited view using less eccentric objects. An ellipse of radius R=15 and eccentricity λ=4 was used for three simulations. For these three cases, the ellipse was oriented at ϕ=0, $\phi=\pi/4$, and $\phi=\pi/2$ respectively. The final limited view simulation used a disc of radius R=15. Noise at a SNR of 0dB was added, and the results are shown in figure 4.6. Accurate estimates were obtained in all four cases, even the previously troublesome case where the ellipse was oriented at

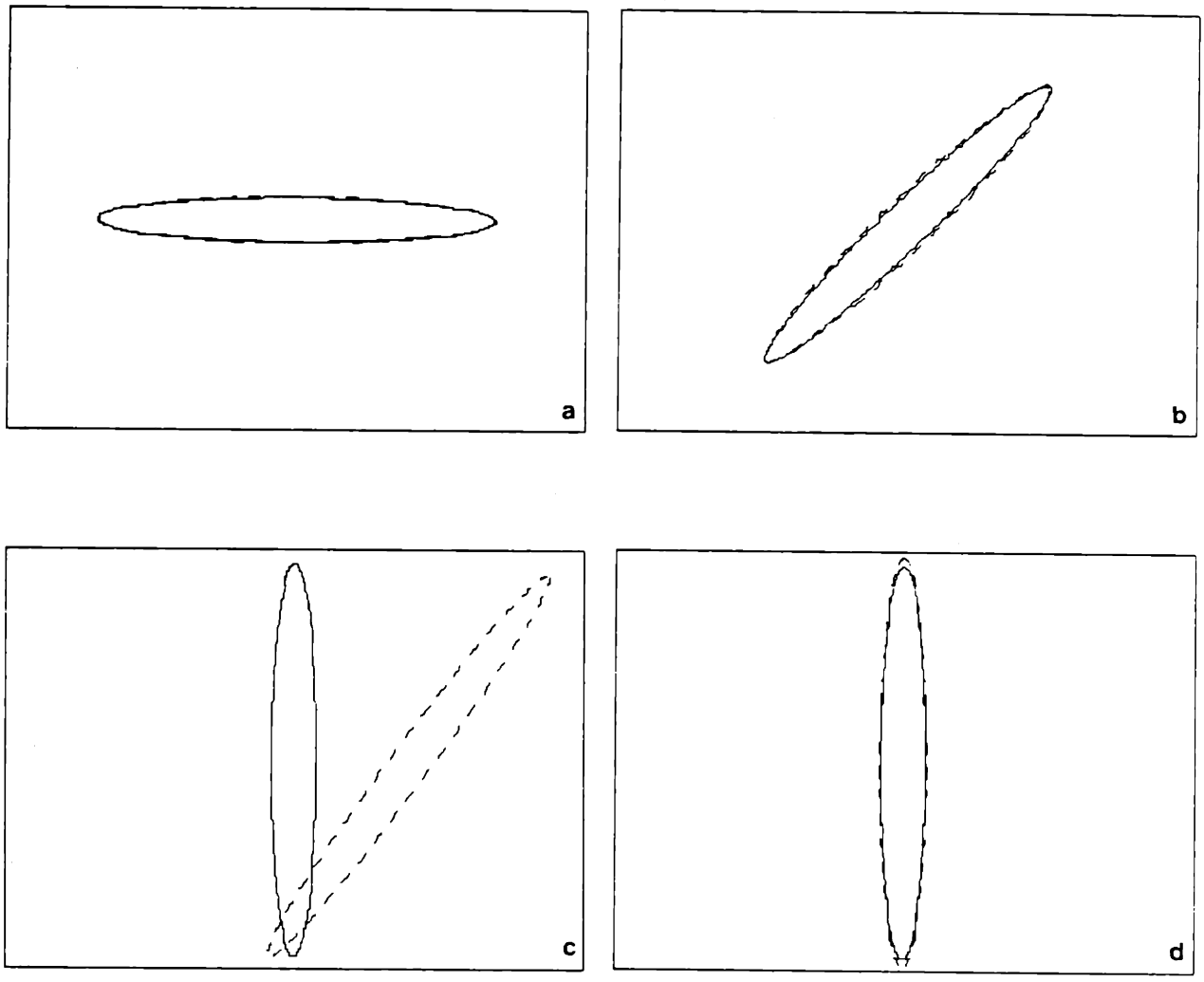

Figure 4-5: Estimation of ellipses (R=10, λ=9) with ϕ=0, $\pi/4$. and $\pi/2$ using limited view measurements

The SNR was 0dB for the first three cases and 8.7 in the final simulation; 31 views 25 rays per view were used to span the view angle of $2\pi/3>\theta>\pi/3$. The final estimates were: a) $\hat{\mathbf{c}}$=(0.0,0.0), $\hat{R}$=10.2, $\hat{\lambda}$=8.6, $\hat{\phi}$=0.0 b) $\hat{\mathbf{c}}$=(0.0,0.0), $\hat{R}$=10.6, $\hat{\lambda}$=7.8, $\hat{\phi}$=45.0 c) $\hat{\mathbf{c}}$=(17.3,-0.84), $\hat{R}$=10.2, $\hat{\lambda}$=12.4, $\hat{\phi}$=54.0 d) $\hat{\mathbf{c}}$=(0.0,0.0), $\hat{R}$=10.4, $\hat{\lambda}$=9.0, $\hat{\phi}$=90.0.

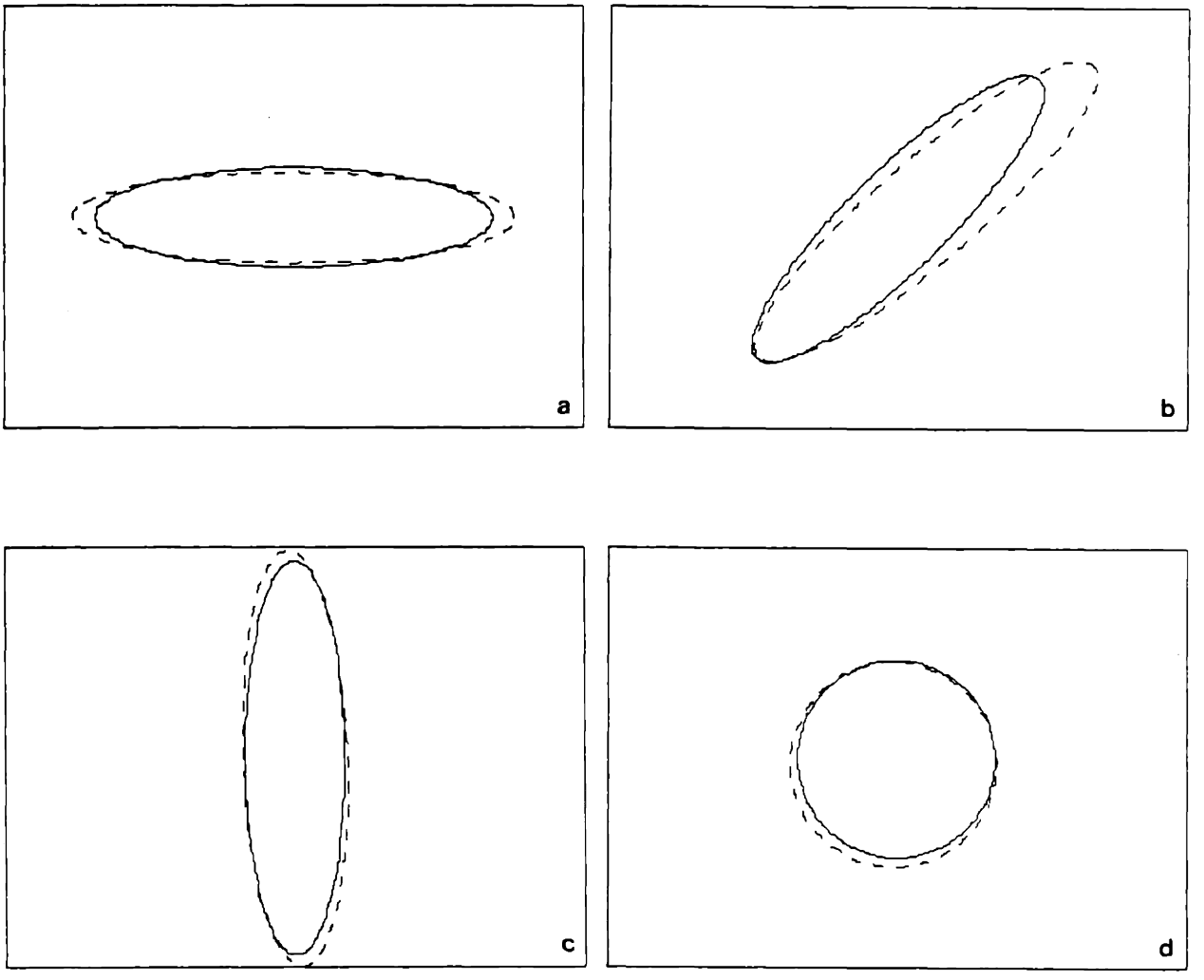

Figure 4-6: Estimation results for four limited view simulations

The first three cases used an ellipse (R=15, λ=4) oriented at ϕ=0, $\pi/4$, and $\pi/2$. In the final case the actual object is a disc with R=15. The SNR was 0dB. The final results were $\hat{\mathbf{c}}$=(0.0,0.0), $\hat{R}$=15.2, $\hat{\lambda}$=4.8, $\hat{\phi}$=0.0° b) $\hat{\mathbf{c}}$=(4.20,1.26), $\hat{R}$=16.0, $\hat{\lambda}$=4.4, $\hat{\phi}$=41.4° c) $\hat{\mathbf{c}}$=(0.0,0.0), $\hat{R}$=15.8, $\hat{\lambda}$=4.0, $\hat{\phi}$=-88.2° d) $\hat{\mathbf{c}}$=(-0.42,-0.84), $\hat{R}$=15.6, $\hat{\lambda}$=1.0.

$\phi=\pi/2$. In these cases, a smaller proportion of the object was spread along the direction of the measurement rays. Thus, these limited measurements provided more information about the object being estimated than they did in the case of the very eccentric ellipse ($\lambda=9$) oriented at $\phi=\pi/2$. The algorithm, therefore, favors more circular objects in these limited view situations.

4.4 Conclusions for Single Object Estimation

In this chapter, we have systematically examined the iterative algorithm's performance for the problem of single object detection and estimation. The results basically showed that this reconstruction method achieves very high levels of performance.

In the full view case, the algorithm's estimates were shown to be very robust to noise, object shape, and sparse data. However, for extreme cases of very little data or data of very poor quality, location and size estimates were the most reliable. The limited view simulations showed that while the algorithm was accurate for most cases, the best performance is achieved when measurements are taken perpendicular to the object's major axis.

Chapter 5
Multiple Object Estimation

The iterative reconstruction method discussed in this thesis focuses on detecting and estimating a single object. This chapter examines what happens when multiple objects are present. Specifically, we examine the case of a density function consisting of two objects, a large primary object and a smaller secondary one. The results of several computer simulations are used to investigate the algorithm's performance.

5.1 Computer Simulations

Three sets of computer simulations were performed. In each case, the primary object was an ellipse of radius R=15, eccentricity λ=4, and orientation ϕ=0. The secondary object was a disc of radius R=10, yielding a size ratio for the two objects of 3/2.

The simulated density fields were constructed by placing the secondary object at various distances along three different rays defined by ϕ=0, $\pi/4$, and $\pi/2$. Thus, the three sets of simulations consisted of the disc located along the ellipse's major axis (ϕ=0), the ellipse's minor axis ($\phi=\pi/2$), and between these axes at $\phi=\pi/4$ (see figures 5.1, 5.2, and 5.3). All of the simulations were noisefree.

These three figures show that when the two objects were sufficiently separated, the secondary object had a very limited effect on the estimation of

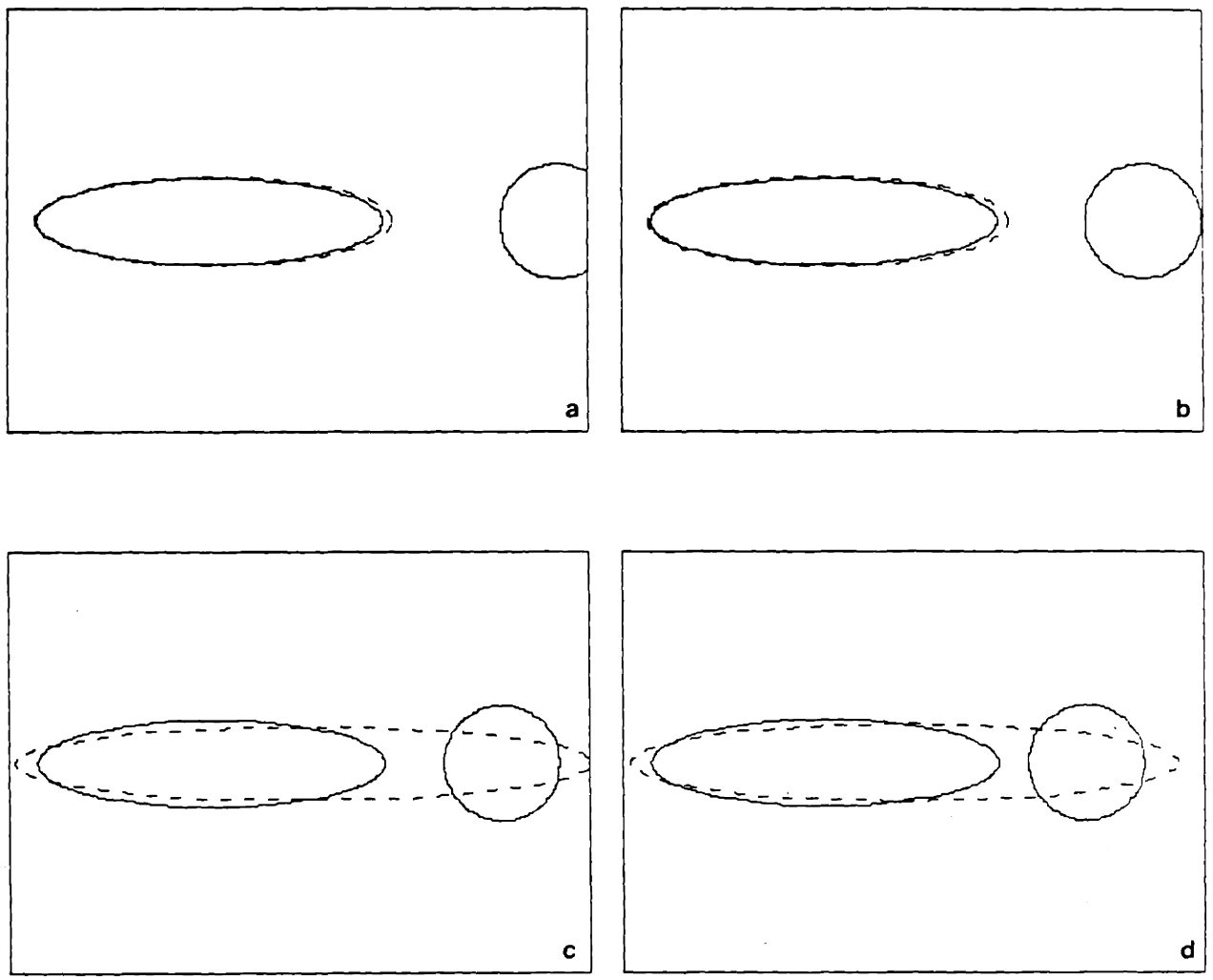

Figure 5-1: Noisefree estimation results for ellipse at $\mathbf{c}$=(-20,0) and disc along ϕ=0.

The true density field (solid line) consisted of an ellipse (R=15, ϕ=0, λ=4) and a disc of radius R=10 at $\mathbf{c}$=(40,0), (35,0), (30,0), and (25,0) respectively. The estimated ellipses for these four cases (dashed line) were a) $\hat{\mathbf{c}}$=(-19.3,0.0), $\hat{R}$=15.4, $\hat{\phi}$=0.0°, $\hat{\lambda}$=4.0; b) $\hat{\mathbf{c}}$= (-19.3,0.0), $\hat{R}$=15.6, $\hat{\phi}$=0.0°, $\hat{\lambda}$=4.0; c) $\hat{\mathbf{c}}$=(-4.2,0.0), $\hat{R}$=17.8, $\hat{\phi}$=0.0°, $\hat{\lambda}$=7.8; d) $\hat{\mathbf{c}}$=(-6.3,0.0), $\hat{R}$=17.8, $\hat{\phi}$=0.0°, $\hat{\lambda}$=7.0.

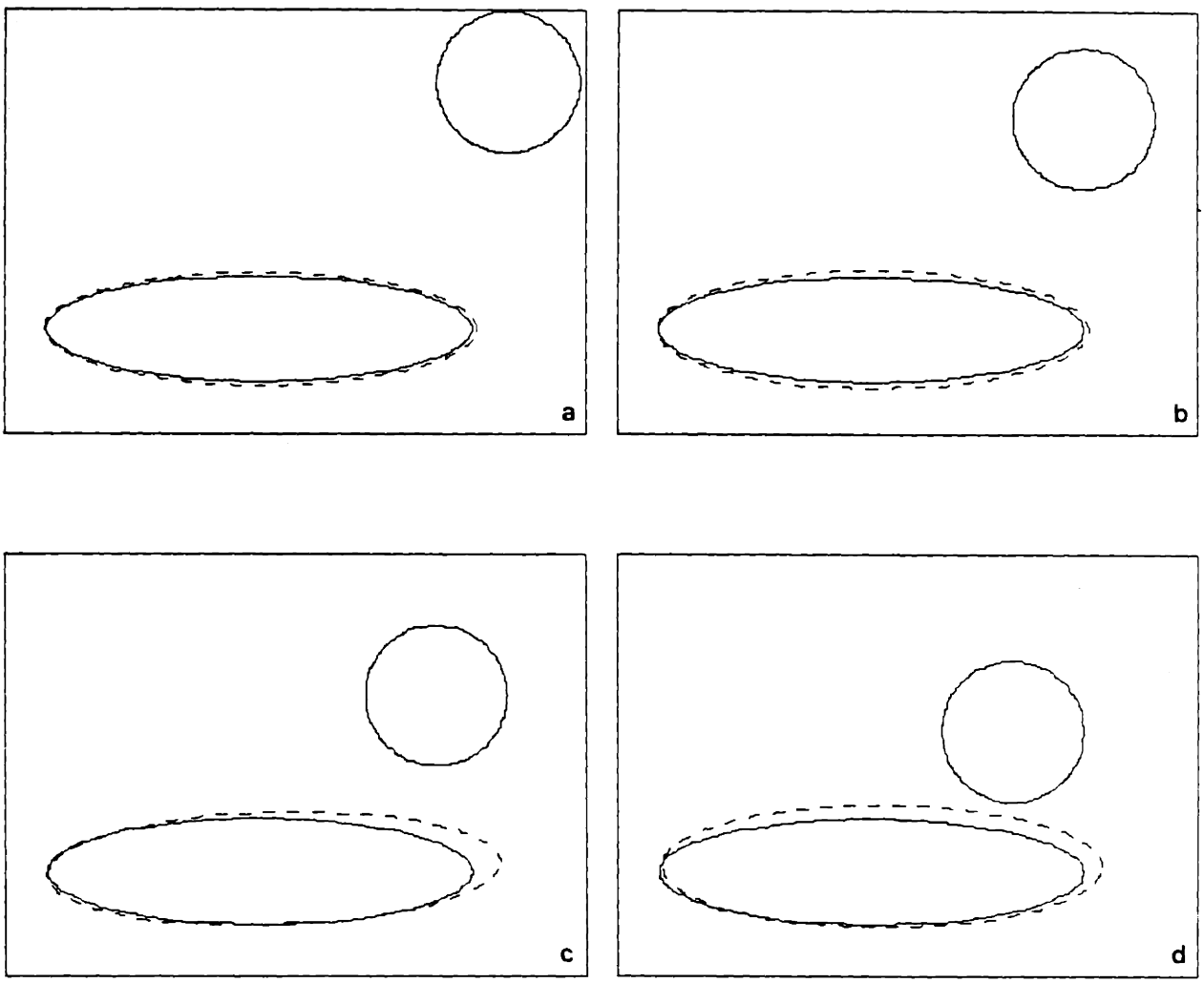

Figure 5-2: Noisefree estimation results for ellipse at $\mathbf{c}$=(-20,0) and disc along $\phi=\pi/4$.

The true density field (solid line) consisted of an ellipse (R=15, ϕ=0, λ=4) and a disc of radius R=10 at $\mathbf{c}$=(15,35), (10,30), (5,25), and (0,20) respectively. The estimated ellipses for these four cases (dashed line) were a) $\hat{\mathbf{c}}$=(-19.7,0.0), $\hat{R}$=15.6, $\hat{\phi}$=0.0°, $\hat{\lambda}$=3.8; b) $\hat{\mathbf{c}}$= (-19.7,0.0), $\hat{R}$=16.0, $\hat{\phi}$=0.0°, $\hat{\lambda}$=3.6; c) $\hat{\mathbf{c}}$=(-18.1,0.42), $\hat{R}$=16.4, $\hat{\phi}$=1.8°, $\hat{\lambda}$=4.0; d) $\hat{\mathbf{c}}$=(-18.5,0.8), $\hat{R}$=16.4, $\hat{\phi}$=0.0°, $\hat{\lambda}$=3.6.

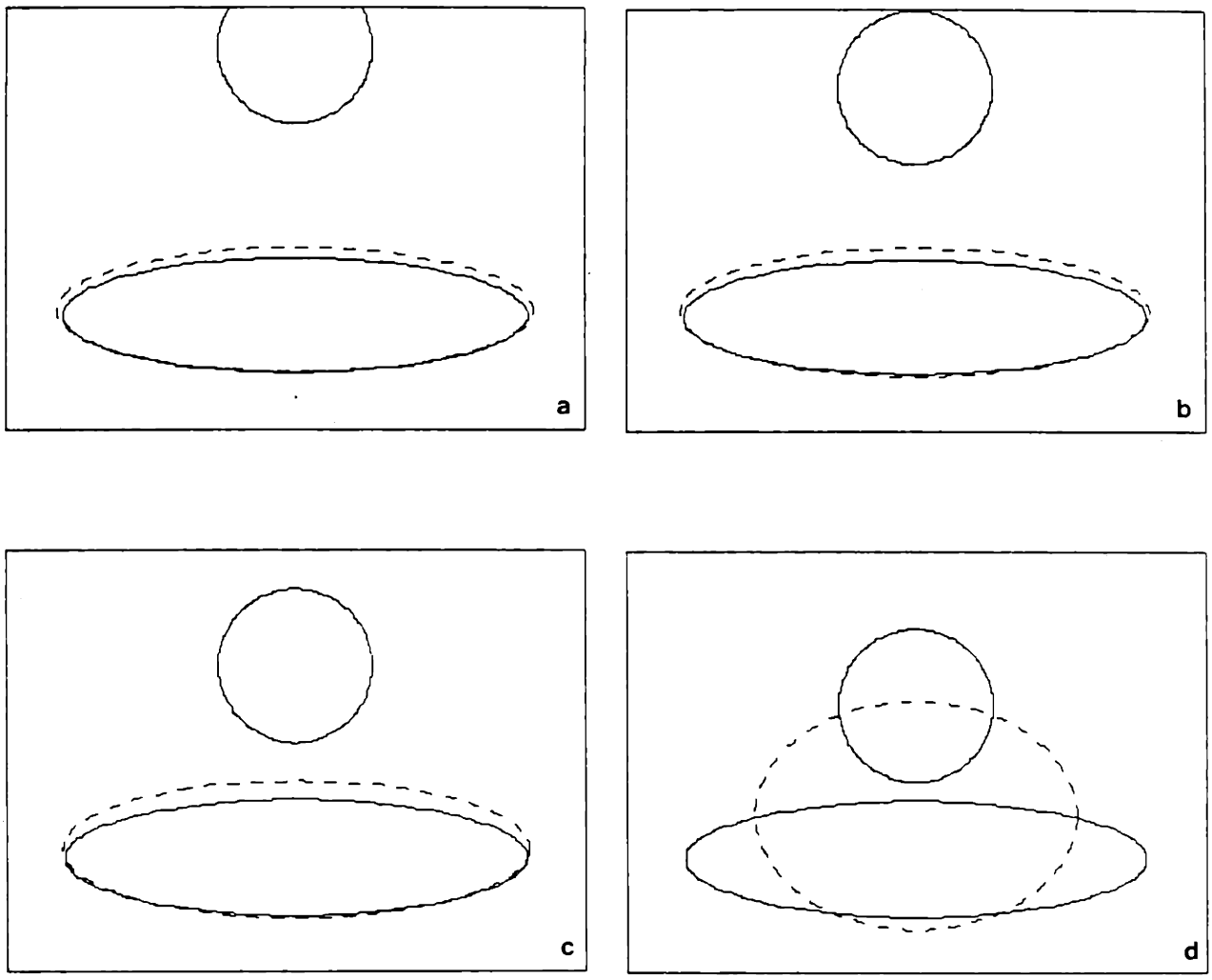

Figure 5-3: Noisefree estimation results for ellipse at $\mathbf{c}=(0,-20)$ and disc along $\phi=\pi/2$.

The true density field (solid line) consisted of an ellipse (R=15, ϕ=0, λ=4) and a disc of radius R=10 at $\mathbf{c}$=(0,15), (0,10), (0,5), and (0,0) respectively. The estimated ellipses for these four cases (dashed line) were a) $\hat{\mathbf{c}}$=(0.0,-19.3), $\hat{R}$=15.8, $\hat{\phi}$=0.0°, $\hat{\lambda}$=3.8; b) $\hat{\mathbf{c}}$= (0.0,-19.3), $\hat{R}$=16.0, $\hat{\phi}$=0.0°, $\hat{\lambda}$=3.6; c) $\hat{\mathbf{c}}$=(0.0,-18.9), $\hat{R}$=16.4, $\hat{\phi}$=0.0°, $\hat{\lambda}$=3.4; d) $\hat{\mathbf{c}}$=(0.0,-14.3), $\hat{R}$=17.6, $\hat{\phi}$=0.0°, $\hat{\lambda}$=1.4.

the primary ellipse. The disc basically exerts a slight "pull" on the estimated object model. When the disc gets close enough to the primary ellipse, the algorithm's final estimate encompasses both objects.

The iterative algorithm essentially attempts to fit the best ellipse to the available data, where the best ellipse is defined in terms of minimizing the two types of area errors mentioned in section 4.2. Thus, two objects are estimated as one when the additional overlap of the secondary object outweighs the penalty associated with the area within the estimated model but outside the true objects.

It is worth noting that in one case, the algorithm did not converge to a final best estimate. For the situation depicted in figure 5.2d, a small limit cycle was reached. The final estimate oscillated with size estimates of $\hat{R}$=16.4 and 16.6 and location estimates of $\hat{\mathbf{c}}$=(-18.49,0.42) and (-18.49,0.84). These computer simulations were set up such that the size quantization was 0.2 and location quantization was 0.42. Thus, this limit cycle is a result of this quantization. The acutal best estimate has $16.6>\hat{R}>16.4$ and $0.84>\hat{c}_2>0.42$. Larger limit cycles were not observed in any of the other simulations.

5.2 Conclusions for Multiple Object Estimation

These computer simulations showed that the iterative estimation algorithm remains very robust to the presence of a sufficiently distant secondary object. In these cases, the estimation of the primary object was only slightly affected.

This robustness suggests the original iterative algorithm could be expanded to include estimating multiple objects. After the primary object is

estimated, its image could be subtracted from the data (i.e. considered part of the background field $f_b(\mathbf{x})$). The next largest object could then be estimated in the same iterative fashion as the first. This process of estimating objects and then subtracting their images from the data could continue until no additional objects were detected. These estimates for the secondary objects could then be used to correct for any bias in the original estimate of the primary object. Figure 5.4 is a block diagram outlining this proposed algorithm for the reconstruction of an density field consisting of multiple objects.

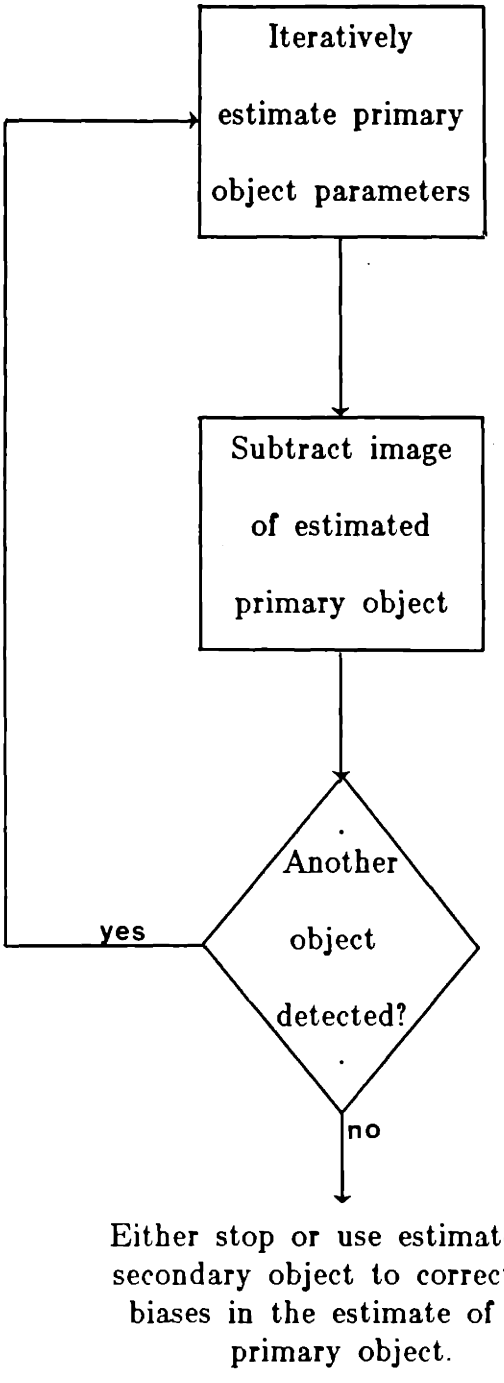

Figure 5-4: Block diagram for multiple object estimation algorithm.

Chapter 6
Conclusions and Areas for Further Investigation

6.1 Conclusions

In this thesis, we described a framework for incorporating a priori information directly into the inverse problem of tomographic reconstruction. Using an object-based stochastic formulation, an iterative algorithm for estimating object location, size, and shape was constructed.

In chapter 2, a field model consisting of the superposition of N objects was detailed. Objects were restricted to the class of ellipses and were paramaterized by a location $\mathbf{c}$, size R, orientation ϕ, and eccentricity λ. This resulted is a finite-dimensional maximum likelihood estimation problem for determining these specific parameters.

The performance of algorithms for the separate estimates of $\mathbf{c}$, R, ϕ, and λ for a single object was examined in chapter 3. While eccentricity estimation required the highest SNR and most data, all of these log likelihood functions were fairly robust to noise, sparse data, and modeling errors. This robustness led to the formulation of an iterative algorithm for estimating the location and geometry of a single object.

Computer simulations were used to analyze the performance of this iterative estimation method for cases consisting of single (chapter 4) as well as multiple object fields (chapter 5). This algorithm was found to be very

accurate in the single object case, even with high noise levels and sparse measurements. For multiple object simulations with a sufficiently distant secondary object, reliable estimates of the primary object were achieved. The robustness to the existence of smaller secondary objects suggested an extention of the original iterative algorithm to include estimating multiple objects.

Overall, the results of this thesis showed that the iterative object-based estimation algorithm is accurate and potentially valuable for a variety of problems. Specifically, the method is attractive for applications where only limited measurements are available, high SNR's are impossible, or the ultimate goal is not a high resolution image but rather the extraction of specific object-related information.

6.2 Areas for Further Investigation

There are several areas open for further research based on the iterative algorithm analyzed in this thesis. A more complex object model could be developed. Using higher order shapes would reduce the errors inherent in assuming everything is elliptical.

Resticting oneself to the class of ellipses, there are still many possible problems to be studied. Specifically, we only considered cases with a maximum of two objects present. Even in the two object case, the algorithm for estimating both objects was only described. Thus, the reconstruction of multiple-object density fields could be examined by implementing the algorithm proposed at the end of chapter 5.

One possible means of analyzing the usefullness of this reconstruction method would be to compare the ability of a human observer to estimate

object shapes based on images generated by conventional reconstruction techniques with the performance of this iterative algorithm. Furthermore, the ideas and techniques presented in this thesis could be tailored to specific applications. The fields of medicine, geophysics and oceanography all provide possible practical problems.

References

Cho, Z.H., J. Burger. 1977. "Construction, Restoration, and Enhancement of 2- and 3-dimensional Images." IEEE Trans. Nucl. Sci. NS-24:886-899.

Drake, Alvin W. 1967. Fundamentals of Applied Probability Theory. McGraw-Hill Book Company, New York.

Hildebrand, F.B. 1976. Advanced Calculus with Applications. Prentice-Hall, New Jersey.

Rossi, David J. 1982. "Reconstruction from Projections based on Detection and Estimation of Objects". Massachusetts Institute of Technology.

Shepp, L.A., B.F. Logan. 1974. "The Fourier Reconstruction of a Head section". IEEE Trans. on Nucl. Sci. NS-21:21-43.

Van Trees, H.L. 1968. Detection, Estimation, and Modulation Theory, part I. John Wiley and Sons, New York.

Van Trees, H.L. 1971. Detection, Estimation, and Modulation Theory, part III, Radar-sonar Signal Processing and Gaussian Signals in Noise. John Wiley and Sons, New York.